MANCHESTER
1824
The University of Manchester

Robotic Tails for Enhanced Mobile Robot Performance

A thesis submitted to the University of Manchester for the degree of
Doctor of Philosophy
in the Faculty of Science and Engineering

2022

Damian Crosby
Department of Mechanical, Aerospace and Civil Engineering

Contents

Word Count: X

List of figures

List of tables

List of publications

Publications go here.

List of abbreviations

AUJ Actuated Universal Joint

2D Two Dimensional

3D Three Dimensional

COM Centre of Mass

DLS Damped Least Squares

DOF Degree of Freedom

PID Proportional Integral Derivative

PI Proportional Integral

PD Proportional Derivative

SHTP Sensor Hub Transport Protocol

MSB Most Significant Bit

LSB Least Significant Bit

I^2C Inter-Integrated Circuit

SPI Serial Peripheral Interface

UART Universal Asynchronous Receiver-Transmitter

DIO Digital Input/Output

IMU Inertial Measurement Unit

GOOP Graphical Object Oriented Programming

CS Chip Select

DFT Discrete Fourier Transform

CPG Central Pattern Generator

ODE Ordinary Differential Equation

GRF Ground Reaction Force

ZMP Zero Moment Point

RMS Root Mean Square

COP Center of Pressure

ADC Analog to Digital Converter

NI National Instruments

PC Personal Computer

PLA Polylactic Acid

IMU Inertial Measurement Unit

PSU Power Supply Unit

TSA Twisted String Actuator

Abstract

This is abstract text.

Declaration of originality

I hereby confirm that no portion of the work referred to in the thesis has been submitted in support of an application for another degree or qualification of this or any other university or other institute of learning.

Copyright statement

Acknowledgements

Acknowledgements go here.

Chapter 1

Introduction

In recent years, there has been a significant increase in the use of mobile robots for industrial, military and service applications, such as moving stock around in warehouses, inspecting equipment in hazardous or remote environments, performing search and rescue operations or acting as infantry support. With advances in battery technology, material fabrication and onboard processing power, mobile robots have been able to fill an increasing number of roles. Modern legged robots such as the *Boston Dynamics* Spot® pictured in figure 1.1 have allowed mobile robots into less rigidly controlled environments, able to navigate rough terrain and stairs. Some of these robots are also incorporating robot arms or other mechanisms that allow them to pick up, carry, and set down payloads. This can be useful for a number of reasons, such as collecting samples from a hazardous environment, clearing away obstructions that impede progress, moving products in a warehouse or providing vital supplies to trapped person. However, payload mass and COM offset is limited not just by the strength of the robot arm, but by the stability of the robot itself. An object that is too heavy, or that is highly unbalanced, will cause the robot to lose stability and fall over, in a similar fashion to a forklift truck or crane.

There are a number of ways this can be mitigated. The *Boston Dynamics* Handle pictured in figure 1.2 robot is a bipedal "wheel-leg" robot designed for warehouse tasks that uses a counterweight that can be swung around the robot body in order to maintain stability. This design, while reasonably effective, is unsuitable for most other mobile robot designs, which are closer to the ground and have four or more legs or wheels. It is also possible to use an adjustable mass on the robot body [1], however the range of compensation that can be pro-

Figure 1.1: Boston Dynamics Spot® working with the Royal Air Force. *Public Domain*

Figure 1.2: Boston Dynamics Handle loading a pallet. © *Boston Dynamics*

vided is necessarily limited by the size of the robot's torso.

One option that has yet to be explored is the use of a robotic tail, in a more traditional sense than the Handle, resembling something closer to what is found in the animal kingdom. Robotic tails of this kind have already been extensively studied for other areas of robot stability, as will be explored in chapter 2.

1.1 Research Concepts

The following section gives an overview of important concepts necessary to understand the issue of mobile robot stability when carrying a payload and the proposed solution.

1.1.1 Mobile Robot Stability

Stability is a significant issue for mobile robot design. Loss of stability can mean the robot is unable to move and must be reorientated or retrieved, which maybe difficult or impossible in some extreme environments, such as in outer space or a nuclear fuel pool. In the worst case it can result in severe damage or destruction of the robot, and any objects it is carrying. This has become more of an issue as mobile robots have become increasingly fast and agile, often running, jumping and hopping around less controlled environments.

In many ways the consequences of stability loss in mobile robots are analogous to other situations. A human that falls over has to pick themselves up before continuing on, or if they are infirm they may require assistance. Likewise they could also suffer injury, or if walking along the edge of a long drop, fall to cause severe injury or death. A forklift truck or other

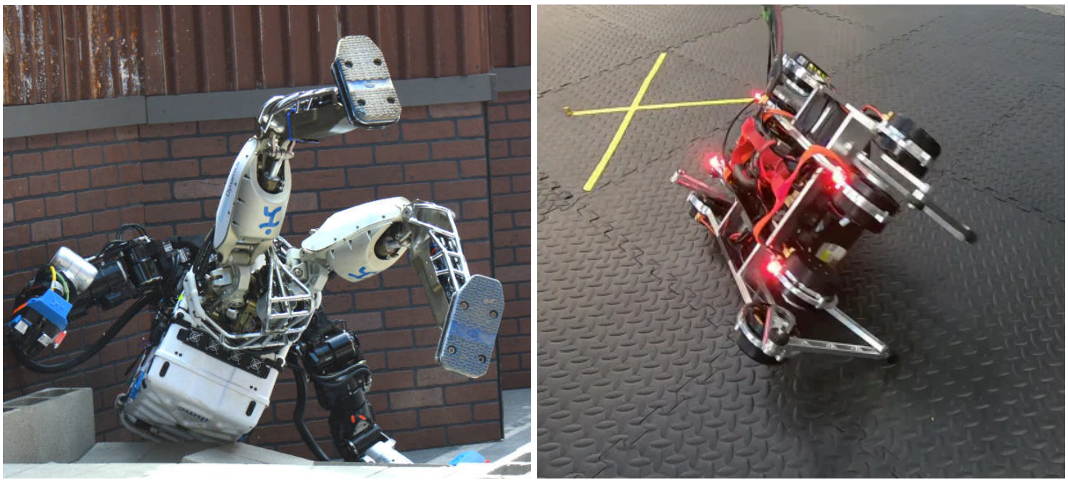

Figure 1.3: Examples of loss of stability in bipedal and quadrupedal robots. *Left Image: Public Domain, Right Image: © Google Robotics*

piece of heavy plant can topple, injuring the driver and causing the damage or destruction of vehicles and materials.

In general, stability from a biomechanical perspective can be divided into two different types, *static* and *dynamic*. While there are numerous ways to define the difference between the two, such as the maximum lyupanov exponent for dynamic stability [2], the following definitions will be used:

- **Static stability** only considers the uniform force of gravity and assumes no other forces are acting on the object.
- **Dynamic stability** considers other forces and torques on the object, both internal and external, as well as gravity.

A stationary object that has no external forces or torques being applied needs to be statically stable, a moving object, or an object that is having a force or torque applied to it other than gravity, needs to be dynamically stable.

Figure 1.4: Examples of loss of stability (static or dynamic) in a human and forklift truck.

1.1.1.1 Static Stability

To determine if the robot is statically stable, the gravity axis projection of the COM needs to fall within a defined "support polygon" on the plane perpendicular to the gravity axis plane, as shown in figure 1.5[1]. The COM can be calculated for using equation 1.1 for n bodies of masses $m_{1...n}$ and COM positions $\boldsymbol{p_{1...n}}$. If the gravity vector is parallel to any of the basis vectors, then the perpendicular components of the COM can be used to determine the static stability.

$$textCOM = \frac{\sum_{i=1}^{n} m_i \boldsymbol{p_i}}{\sum_{i=1}^{n} m_i} \tag{1.1}$$

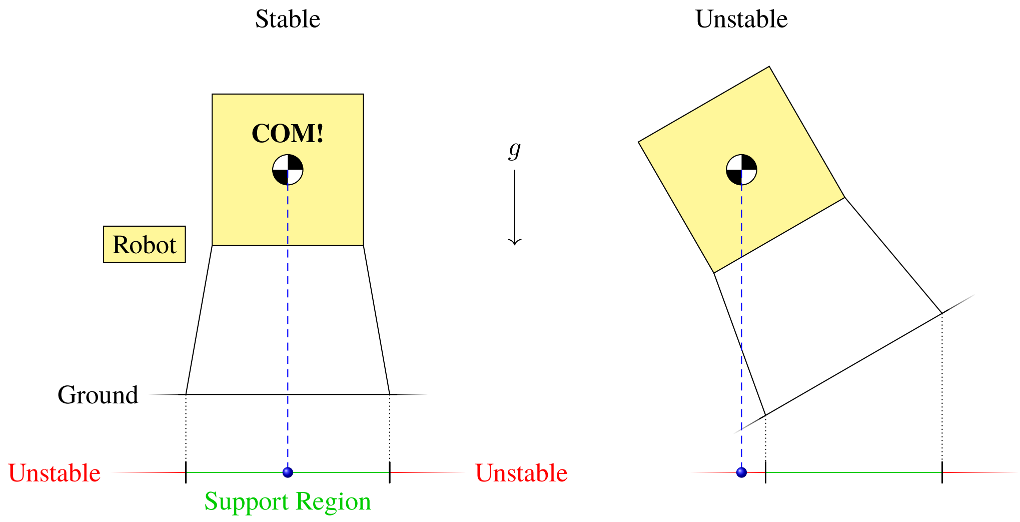

Figure 1.5: 2D representation of the static stability of a legged robot, with the support region defined by the contact points of the legs with the ground. Notice how the orientation of the robot with respect to the gravity axis can move it in and out of the static stability region.

Fundamentally, there are two different methods to maintain static stability:

- Change the region or shape of the support region so the gravity axis projection of the COM remains within the bounds of the support region.
- Move the gravity axis projection of the COM so it remains within the bounds of the support region.

The former method can be considered equivalent to using a walking pole to steady yourself on uneven ground when hiking, the leg of the pole acts as a new vertex that is used to calculate the support polygon, expanding it sufficiently, or placing your foot in front of you when walking. The latter method can be considered equivalent to leaning back to remain upright when falling forward. Leaning back moves the centre of gravity to keep it within the support polygon.

However, just because the COM falls outside of the support polygon does not mean that loss of stability is inevitable, as long as a force or torque applied to the body counteracts the forces and torques induced by the force of gravity in order to maintain stability. This is similar to applying a torque to your ankle when standing on one leg, or a strong wind keeping

[1] Centre of Mass and Center of Gravity are used interchangeably here. This assumes a uniform gravitational vector g, which is a suitable assumption for terrestrial robots due to the overwhelming dominance of the earth's gravitational field. If there is a non-uniform gravitational field, then the Centre of Mass and Center of Gravity will not be equivalent, and the terms can not be used interchangeably.

you upright when leaning forward. If this is the case, then *dynamic* stability is maintained while *static* stability is lost. If the force or torque is removed, then stability is lost. Conversely, forces and torques can also cause loss of stability even if the center of gravity does not fall outside of the support polygon. This is similar to being pushed over, or stopping too quickly and falling forward. So dynamic stability can maintain stability even if static stability is lost, but static stability cannot maintain stability if dynamic stability is lost.

1.1.1.2 Dynamic Stability

To determine if the robot is dynamically stable, it is not enough to only consider the position of the gravity axis projection of the COM, as it is for static stability. This is where the concept of the ZMP [3] is useful for mobile robots to check if dynamic stability will be maintained. It extends the calculation used for static stability by including inertial forces caused by accelerations of the bodies, as shown in figure 1.6. Though it has mostly been utilised for bipedal robots to ensure stability while walking, it is also applicable to quadruped robots [4]–[6], and has even been investigated for the development of a stability warning system in road vehicles [7]. The ZMP is formally defined as the point at which the point where the total of horizontal inertia and gravity forces equals zero. It can be thought of as a *dynamically augmented* version of the gravity axis projection of the center of mass. Equation 1.2 defines the position of the ZMP for a robot or vehicle with n bodies of masses $m_{1\dots n}$, COM positions $\boldsymbol{p_{1\dots n}}$ and COM accelerations $\boldsymbol{\ddot{p}_{1\dots n}}$, in contact with a planar surface of normal vector $\boldsymbol{n}$ (ZMP cannot be calculated for non-planar surfaces). $\boldsymbol{\tau_{i\dots n}}$ defines the torque acting on each COM, which can be calculated from .

$$
\begin{aligned}
\boldsymbol{\tau_i} &= \boldsymbol{R_i}\left(\boldsymbol{I_i}\ddot{\theta}_i - \left(\boldsymbol{I_i}\dot{\theta}_i\right) \times \dot{\theta}_i\right) \\
\text{ZMP} &= \frac{\boldsymbol{n} \times \sum_{i=1}^{n} \left(\boldsymbol{p_i} \times m_i \boldsymbol{g} - \boldsymbol{p_i} \times m_i \boldsymbol{\ddot{p}_i} - \boldsymbol{\tau_i}\right)}{\boldsymbol{n} \cdot \left(\left(\sum_{i=1}^{n} m_i \boldsymbol{g}\right) - \left(\sum_{i=1}^{n} m_i \boldsymbol{\ddot{p}_i}\right)\right)}
\end{aligned}
\tag{1.2}
$$

1.1.1.3 Addition of a Payload

When a payload is added to the robot, it is equivalent to instantaneously adding an extra body to the robot of mass m_p and position p_p thus changing the COM. Initially the payload will also create an extra contact point with the ground, changing the support polygon so the robot remains statically stable. However, as soon as contact between the payload and ground is severed, the robot can become statically unstable, as shown if figure 1.7. This does not mean the robot will immediately lose stability, the dynamic forces created picking up the payload may keep the robot dynamically stable, but once the robot is stationary without other forces acting upon it, it may lose stability. The best way to compensate for this is to change the position of the other bodies so the COM remains within the support polygon.

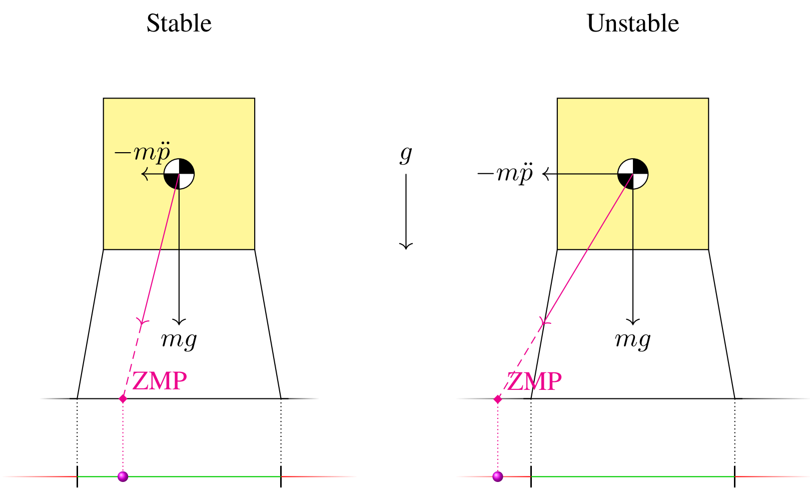

Figure 1.6: 2D representation of the ZMP of a legged robot under horizontal acceleration, with the support region defined by the contact points of the legs with the ground. Notice how increasing the horizontal acceleration of the robot can make it dynamically unstable.

This is akin to leaning back when carrying something heavy, but leaning generally has limited range, so can only compensate for lighter payloads.

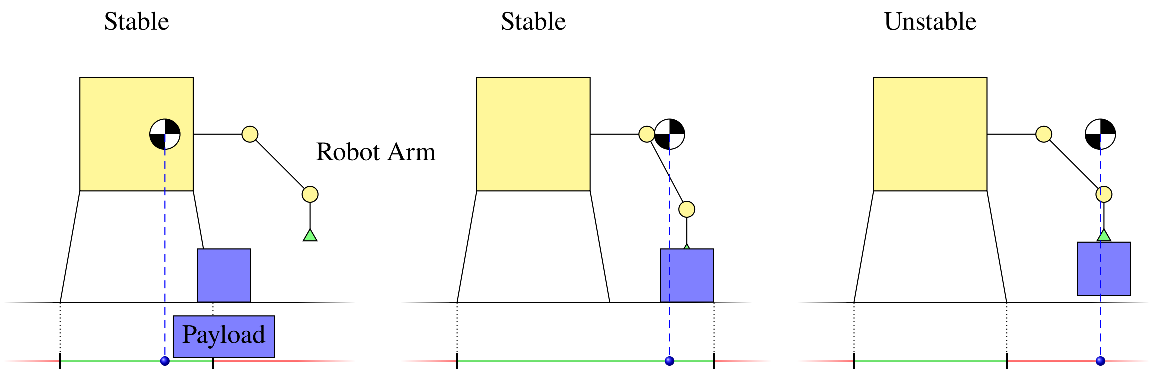

Figure 1.7: 2D representation of the static stability of a legged robot picking up a payload, with the support region defined by the contact points of the arm and legs with the ground. Notice how the payload acts as a contact point until it is lifted off the ground, preventing loss of stability even as the COM is translated due to the mass of the payload.

1.1.2 Studies of Tails in Animals

Tails are a common sight in vertebrate animals, a natural extension of the spinal column. While some tails are used purely for grasping, communication or decoration, many have significant function in maintaining stability during locomotion. The following research studies demonstrate the importance of the tail for stability in two animals, by measuring their performance before and after surgical operations to disable the function or remove their tail.

1.1.2.1 Balancing Ability of a Cat Before and After Partial Tail Paralysis

In [8], experiments were conducted domestic cat uses its tail for balance when walking along a narrow beam, which was shifted laterally at a certain velocity by $2.5\,\text{cm}$ or $5\,\text{cm}$ while they are traversing it. Four cats were trained to walk across the beam, before and after a surgical procedure that severed the nerves in the spinal cord just above the tail, severely affecting its function by causing paralysis of the tail muscles. As can be seen from figure 1.8, this procedure caused the cats to fall from the beam far more often than before surgery.

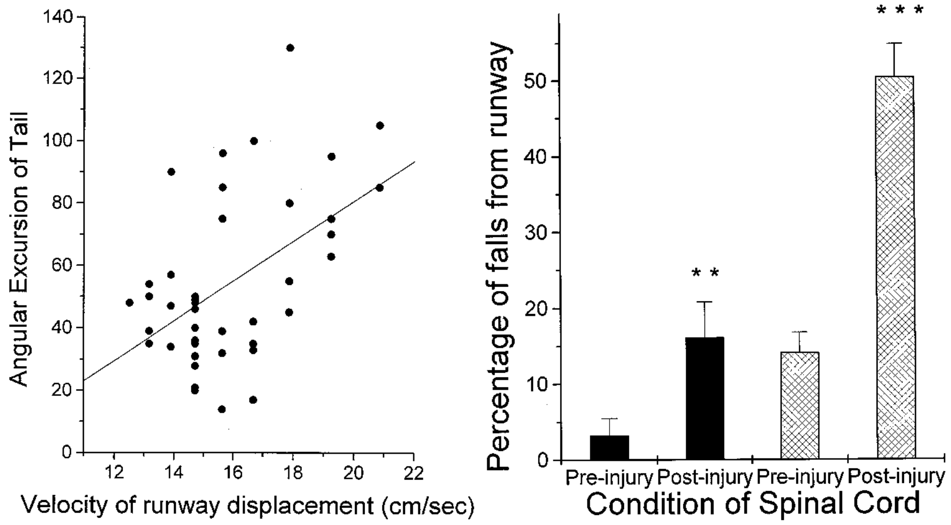

Figure 1.8: Charts from [8] showing how the cat's tail is used to maintain balance on the beam when it is shifted, and how impairing it causes a major loss of stability. Dark bars are a 2.5 cm displacement, cross-hatched bars are a 5 cm displacement.

1.1.2.2 Aerial Stability of a Jumping Lizard Before and After Tail Removal

In [9], the aerial stability of the arboreal lizard is examined, with an intact tail and with their tail removed. Lizards with the tail removed are unable to maintain their body orientation and do not land cleanly, as can bee seen in figure 1.9.

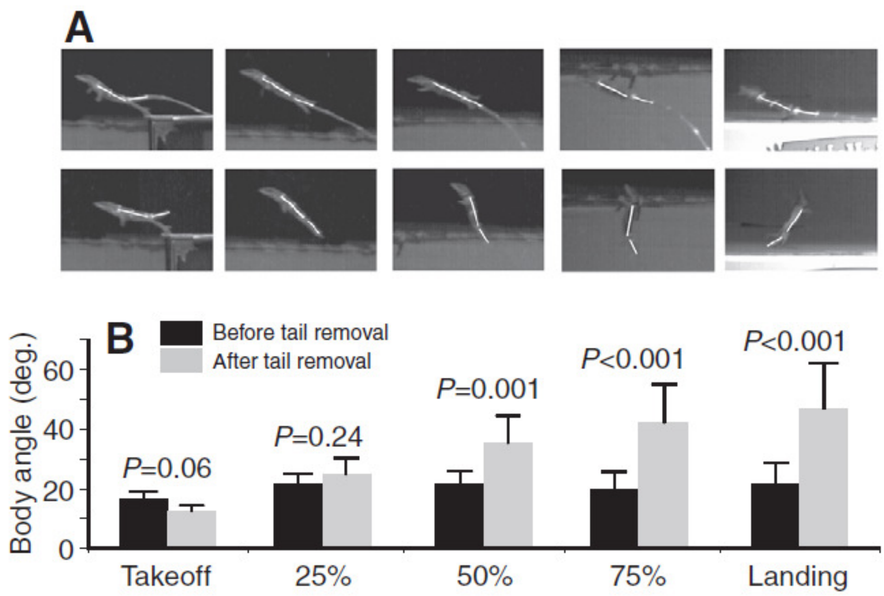

Figure 1.9: Image from [9], showing the body angle of a lizard during a jump, before and after tail removal. Section A shows still frames of the lizard at various stages when jumping, with the spinal column highlighted. Section B shows the resulting body angle at these snapshots.

1.2 Aims and Objectives

This research investigates the use of a robotic tail in maintaining the static stability of a mobile robot when carrying a payload. This is done by measuring the stability of a robotic system when carrying a payload using a robotic arm, with and without the addition of a robotic tail designed to adjust the COM to maintain stability. In order to accomplish this, a number of different strands of research need to be brought together. The following key objectives are required:

- Investigate the current uses of robotic tails in mobile robots in order to gain insight into further research.
- Investigate potential actuation methods for the robotic tail.
- Design a configurable payload that can simulate a range of mass and COM.
- Investigate if there is any advantage to using a multi-segmented tail.
- Design a system that can measure stability in a way that could be easily used on a mobile robot platform.
- Compare the stability performance of a system that is able to pick up, carry and set down the payload with and without an active tail that uses the measured stability as a closed loop control signal.

1.3 Thesis Organisation

The rest of this thesis is organised into the following chapters:

Chapter 2: A Literature Review of Terrestrial Robots with Robotic Tails and Their Functions This chapter conducts a "state of the art" review into the existing literature for robotic tails on mobile robots, with an eye towards robot stability.

Chapter ??: ?? This chapter proposes and experimentally validates a potential design for the tail actuator, based on the Twisted String Actuator.

Chapter 3: Creating a Configurable Payload for Instability Experiments This chapter describes the design and examines the performance of a dummy payload that can have its mass and COM easily adjusted.

Chapter ??: ?? This chapter simulates single and multiple segment tails of the same mass controlling their COM (which is what contributes to static stability, as mentioned in section), which answers secondary question *4* for the specific application in the primary research question.

Chapter 4: Investigating the use of a 2DOF Pendulum Tail for Compensating for Instability when Carrying a Payload This chapter describes the design of a static rig that uses a measures stability using load cells, using a design that could be easily adapted to the majority of mobile robots, answering secondary question *1*. Then it proceeds to test the efficacy of the chosen tail design by using a robot arm to carry various configurations of the payload designed in chapter 3 answering the primary research question.

Chapter ??: ?? This chapter examines the findings from the previous chapters and considers the impact of the research. It also examines some of the limitations and proposes future work not covered in other chapters.

References

[1] M. Gor, P. Pathak, A. Samantaray, J.-M. Yang, and S. Kwak, "Fault accommodation in compliant quadruped robot through a moving appendage mechanism," *Mechanism and Machine Theory*, vol. 121, pp. 228–244, 2018.

[2] A. Ekizos, A. Santuz, A. Schroll, and A. Arampatzis, "The maximum lyapunov exponent during walking and running: Reliability assessment of different marker-sets," *Frontiers in physiology*, p. 1101, 2018.

[3] M. Vukobratović and B. Borovac, "Zero-moment point—thirty five years of its life," *International journal of humanoid robotics*, vol. 1, no. 01, pp. 157–173, 2004.

[4] H. Montes, S. Nabulsi, and M. Armada, "Detecting zero-moment point in legged robot," in *Climbing and Walking Robots*, Springer, 2005, pp. 229–236.

[5] T. Akbas, S. E. Eskimez, S. Ozel, O. K. Adak, K. C. Fidan, and K. Erbatur, "Zero moment point based pace reference generation for quadruped robots via preview control," in *2012 12th IEEE International Workshop on Advanced Motion Control (AMC)*, IEEE, 2012, pp. 1–7.

[6] A. W. Winkler, F. Farshidian, D. Pardo, M. Neunert, and J. Buchli, "Fast trajectory optimization for legged robots using vertex-based ZMP constraints," *IEEE Robotics and Automation Letters*, vol. 2, no. 4, pp. 2201–2208, 2017.

[7] S. Lapapong, A. Brown, and S. Brennan, "Experimental validation of terrain-aware rollover prediction for ground vehicles using the zero-moment point method," p. 6, Oct. 2020.

[8] C. Walker, C. J. Vierck Jr, and L. A. Ritz, "Balance in the cat: Role of the tail and effects of sacrocaudal transection," *Behavioural brain research*, vol. 91, no. 1-2, pp. 41–47, 1998.

[9] G. B. Gillis, L. A. Bonvini, and D. J. Irschick, "Losing stability: Tail loss and jumping in the arboreal lizard anolis carolinensis," *Journal of Experimental Biology*, vol. 212, no. 5, pp. 604–609, 2009, ISSN: 0022-0949. DOI: 10.1242/jeb.024349. eprint: https://jeb.biologists.org/content/212/5/604.full.pdf. [Online]. Available: https://jeb.biologists.org/content/212/5/604.

Chapter 2

A Literature Review of Terrestrial Robots with Robotic Tails and Their Functions

In this chapter, a literature review methodology is described that produces a collection of relevant publications in the field of terrestrial mobile robots with tails. A categorisation system is developed based on the function of the tail and how it contributes to the robot's dynamics. In each category, selected publications are then summarised with accompanying figures from the source material. In the discussion, broader findings about the qualities of the robot tails found in the literature are explained, which include what performance comparisons were made between different tail designs, motions, or control methods within the same publication for the same tail function, any bio-inspiration the publication took from the animal kindgom, be it through direct performance comparsion, or loose "inspiration", and finally whether multiple segments confer any performance advantage in specific tail applications.

2.1 Introduction

The field of terrestrial robots with robotic tails is incredibly diverse, reflecting the many functions of tails in the animal kingdom. Even discounting tails used for fluid dynamics, e.g. swimming, water walking and flying robots, and focusing only on robots that use their tail during "terrestrial" locomotion, broadly defined as when a robot is moving along a contiguous surface, or jumping from one surface to another surface, there are many applications of robotic tails. In order to make sense of the state of the field, an abstract categorisation system is considered based on the environment the robot is in when the tail is active, the specific action the robot is taking to move itself in space, and what the specific function of the tail is with respect to the robot dynamics. Using this categorisation system, various examples are explored from a set of research articles selected using specific keywords. From this, conclusions can be derived about the general design and operation of robotic tails, which can be used to influence and guide the research covered in chapters **??**.

2.2 Literature Review Methodology

Using three online publication repositories, *IEEE Xplore*, *Scopus* and *Web of Science*, a search query was conducted to find relevant publications. The query was tailored to include all publications with **tail*** or **appendage** in the title along with **robot*** (***** indicates a wildcard suffix), but to exclude publications that concerned swimming, water walking, or flying robots, as using a tail as a rudder to influence fluid dynamics was outside of the scope of the research. Further exclusions were added upon experimentation with the query in order to remove false positives in areas such as chemistry (as molecules are often described as having "tails") or medicine (as it did not pertain to mobile robots and usually concerned biological structures such as proteins and cells). The date range was set from January 1980 to June 2021, when the search was conducted, to exclude outdated publications:

> (Tail* **OR** Appendage) **is contained in** *Document Title* & Robot* **NOT** (Fish **OR** Swim) **NOT** (Surgery **OR** Medic* **OR** Tumour) **NOT** (Helicopter **OR** Unmanned Aerial Vehicle **OR** UAV) **NOT** Underwater **NOT** (Chemical **OR** Chemistry) **NOT** Tailor* **is contained in** *Document Title*

As a result **498** publications were discovered. After duplicates were removed and after screening abstracts and full texts, a total of **84** unique publications were selected for inclusion. A flowchart of this process can be found in figure 2.1.

The final selection included 55 *experimental* publications, which included experimental results from a physical prototype, and 29 *simulation* publications which only included results from dynamics simulations and/or analytic functions. This review will focus on experimental publications, as they have stronger evidence for the efficacy of their research.

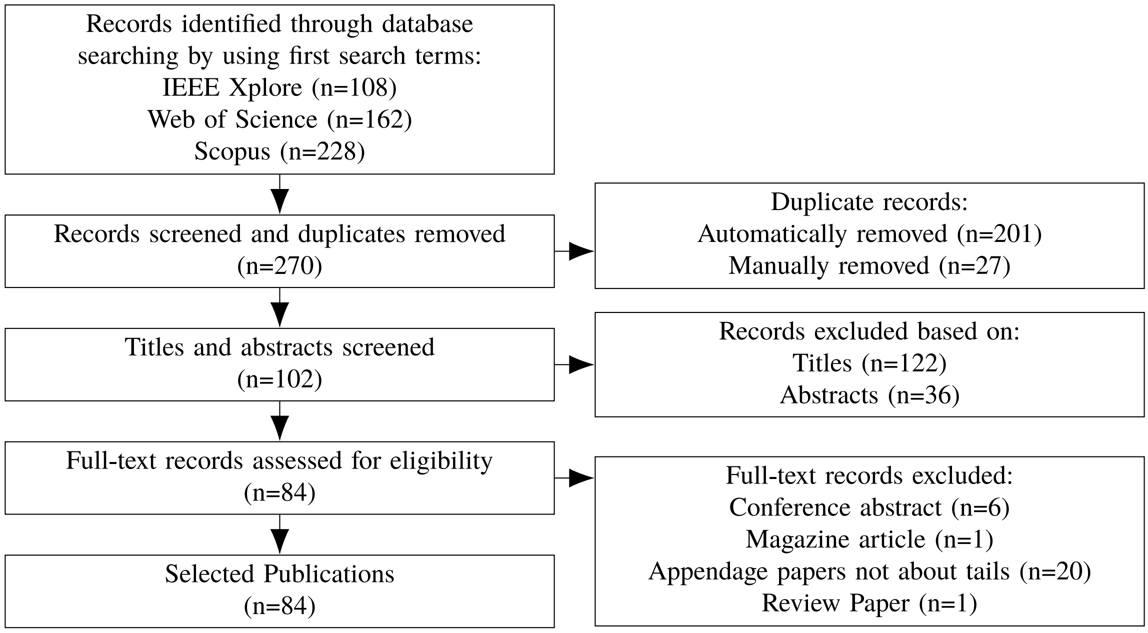

Figure 2.1: PRISMA Flowchart of the publication selection process.

2.3 Tail Functions of Terrestrial Robots

2.3.1 Categorisation System

The resulting publications represented a wide array of different robot designs and multiple forms of locomotion. Therefore, a simple categorisation system was required in order to better understand the majority of the functions of these tails. After careful analysis of the literature, two questions could be asked that provided common answers:

1. Is the robot on the ground, in the air or transitioning between those states when the tail is active?
2. What precisely is the robot doing when the tail is active?
3. What does the tail do to the dynamics of the robot (i.e. what would happen if there *wasn't* a tail present)?

Each question can then assign a tiered category to a publication based on the answer, the three tiers named *Environment*, *Action* and *Function*.

1. **Environment:** The general domain the robotic system is operating in when the tail is active. From the reviewed literature, three categories have been created:
   - *Terrestrial:* A robot with an active tail when the robot is touching a surface, such as a robot driving along the ground.
   - *Aerial:* A robot with an active tail when the robot is in free space, such as a robot which *has jumped* into the air, or is falling off a ledge.

- *Transition:* A robot with an active tail when the robot is just about to transition from between the two previous environments, such as a robot *just about* to jump into the air.

2. **Action:** The specific action the robot is performing when the tail is active. Most actions are unique to each environment, except for *hopping*.

   - *Straight:* A robot travelling across a surface maintaining its direction of travel.
   - *Accelerating:* A robot changing its velocity in the direction of travel across a surface. In the literature, this was a robot coming to complete stop, and starting from stationary.
   - *Turning:* A robot changing its direction of travel across a surface, such as a robot turning a corner.
   - *Balancing:* A robot undergoing external disturbances while travelling across a surface, typically due to adverse terrain, such as a robot navigating a rough and uneven surface without falling over.
   - *Hopping:* A robot executing a sequence of periodic jumps in order to travel across a surface, similar to the method of locomotion of a Kangaroo.
   - *Jumping/Falling:* A robot executing isolated non-periodic jumps, falling off a ledge or launching off a ramp, typically to transition from one surface to another at a different altitude and/or orientation.

3. **Function:** The purpose of the tail when the robot is performing the action. These categories usually apply to multiple actions.

   - *Stability:* The tail is used to *maintain* some aspect of the robot's position and/or orientation from the start of the action.
   - *Initiation:* The tail is used to *change* some aspect of the robot's position and/or orientation from the start of the action.
   - *Amplification:* The tail is used to *amplify* the effects of an action by other parts of the robot (such as the legs) which changes the position and/or orientation.

For example, a robot with a tail that helps it increase its apex when hopping, is in the *Transition* environment as it is about to transition from being on the ground to in the air when the tail is active. The robot itself locomotes by hopping, so it is performing a *Hopping* action, and since without the tail the robot would still be capable of hopping, but would not have such a tall apex, the tail can be considered to be performing *Amplification* of the robot's existing capabilities. Overall, this results in the categorisation *Transition* → *Hopping* → *Amplification*.

Another example is a robot with a tail that prevents it from falling over on rough terrain. The robot is in the *Terrestrial* environment as it is on the ground when the tail is active.

The robot itself is performing a *Balancing* action as it is trying to remain upright during locomotion, and since without the tail the robot would fall over, the tail can be considered to be maintaining the *Stability* of the robot. Overall, this results in the categorisation *Terrestrial* $\rightarrow$ *Balancing* $\rightarrow$ *Stability*.

This categorisation system does not include robots that have a tail but are not mobile, or where the tail is used for non-locomotion tasks, such as self righting [1] or dragging objects [2]. It also does not include robots where the tail is in constant contact with the ground as essentially an extra leg [3].

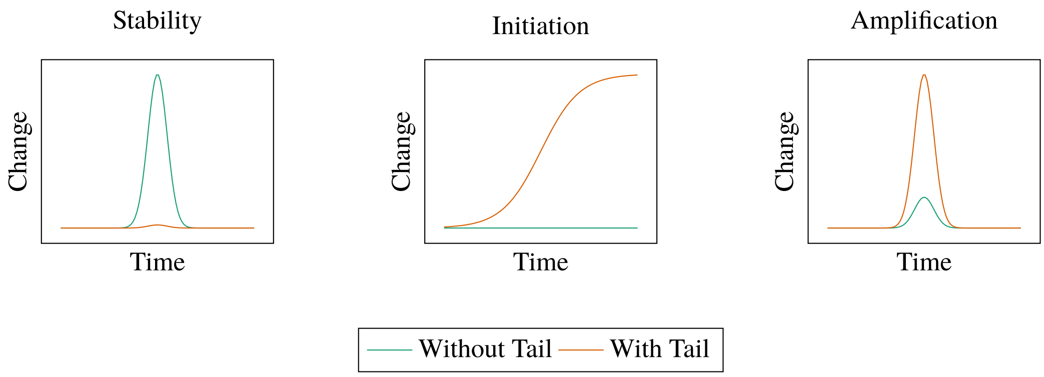

Figure 2.2: Abstract graphs of the different functions of the tail, with the magnitude representing some kind of change in the robot's position and/or orientation.

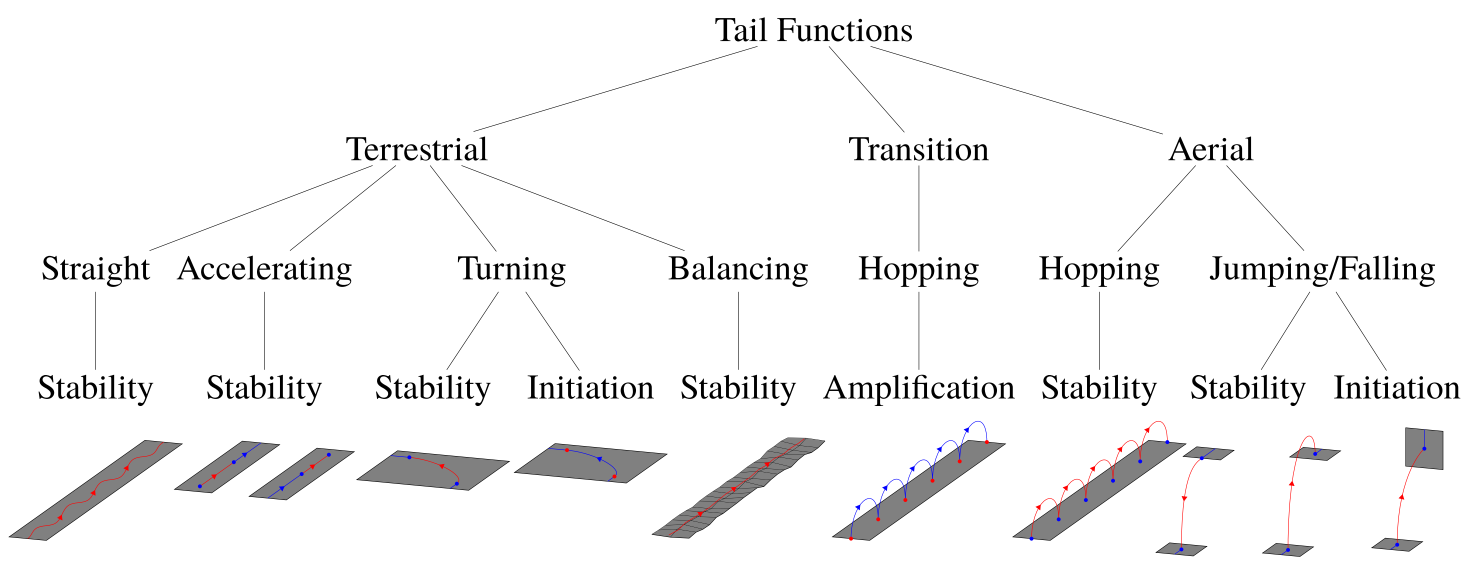

Figure 2.3: Tree diagram of all the categorisations found in the publications with accompanying visual diagrams.

2.3.2 Examples from each Category

2.3.2.1 *Terrestrial → Straight → Stability*

[4] uses a quadrupedal robot with a gait controlled by a Central Pattern Generator (CPG).

Upon initial experiments with a trotting locomotion with no active tail, the robot would not maintain a set heading, it would instead slowly begin to drift in a circle. Visual observations noted that the robot would topple onto its front left leg that was in "swing" phase (lifted off the ground), and it would drag on the ground until in "stance" phase. This resulted in a difference between the Ground Reaction Force (GRF) of the left and right feet which caused the drift in locomotion path.

By implementing a swinging tail that imparted an opposing torque to the direction of the topple, the differences between the left and right GRF were reduced, and the robot could maintain its heading, as can be seen in figure 2.5.

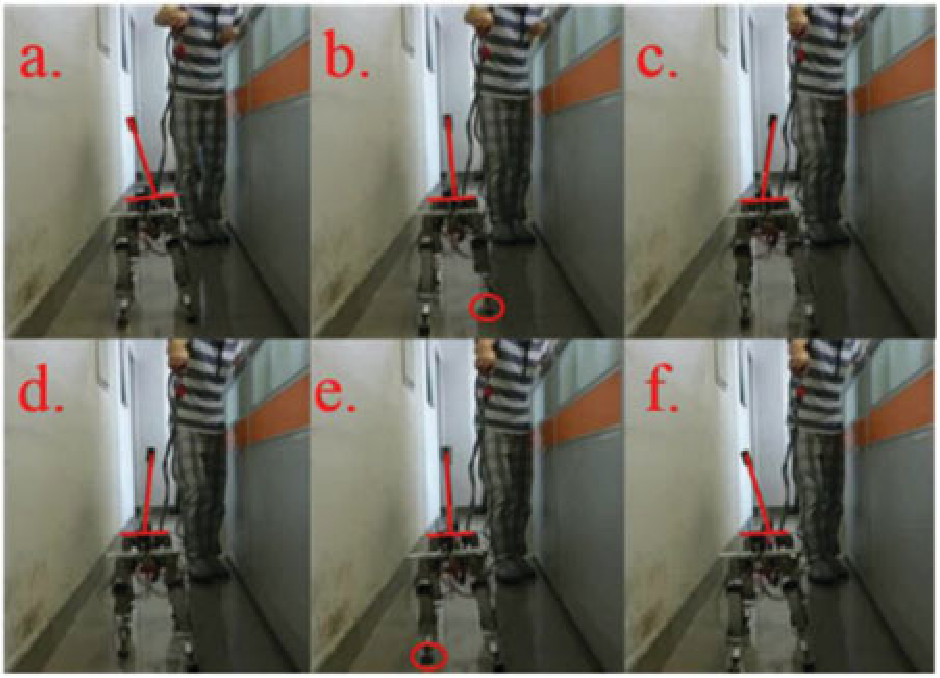

Figure 2.4: Image from [4] showing how the tail moves during the gait in order to correct for heading drift.

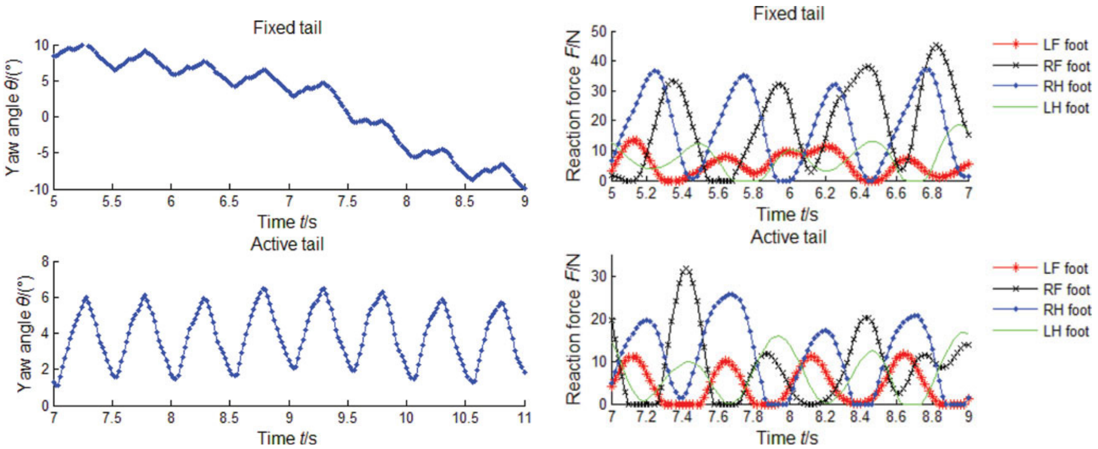

Figure 2.5: Data from [4] showing the effects of a static and dynamic tail on maintaining robot heading in a trotting gait.

2.3.2.2 *Terrestrial → Accelerating → Stability*

[5] used inspiration from the Cheetah to improve the acceleration and braking capabilities of a wheeled robot. The research is based on findings from [6], which shows that quadruped acceleration and deceleration in the animal kingdom is limited by their ability to constrain body pitch to prevent toppling over. It can be considered analogous to a motorcycle: accelerate too fast and the vehicle will "pop a wheelie" and potentially flip backwards, decelerate too fast and the opposite may occur.

Using a combined state feedback and Proportional Integral (PI) controller based on the angular position of the tail, and the angular velocity of the tail and body, the researchers were able to increase the acceleration and braking capabilities of the robot by using the tail to generate an opposing torque to the direction of body pitch, as can be seen in figure 2.8. This was verified by running a series of experiments, increasing the acceleration/braking magnitude until the robot failed to complete the test by toppling over.

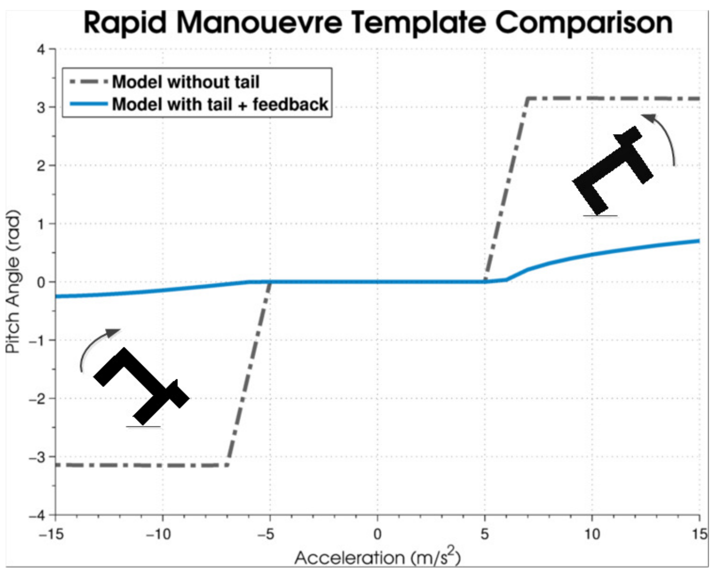

Figure 2.6: Simulation Data from [5] showing the how the body pitch would be reduced when accelerating of braking with an active tail.

Figure 2.7: Images from [5] showing the robot performing a rapid acceleration test with the tail.

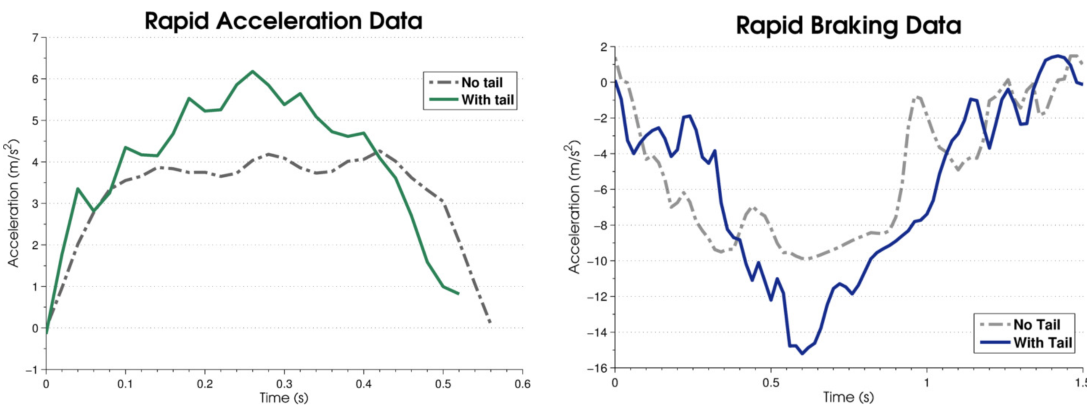

Figure 2.8: Experimental Data from [5] showing the maximum acceleration achieved with and without an active tail.

2.3.2.3 *Terrestrial → Turning → Stability*

[7], [8] took similar inspiration from the Cheetah to allow for tighter turns by allowing greater lateral acceleration. [7] swings the tail out in a single motion in the direction of the turn, producing an opposing torque to the centrifugal force that would otherwise topple the robot during the turn. In contrast, [8] moves the tail constantly in a conical motion, the direction of rotation in the direction of the turn. This also produces an opposing torque in the same fashion, but was not limited in duration, as in the first strategy the tail would eventually contact the ground. This allowed for turns of longer duration to be stabilised.

The control system and experimental procedures were similar to those in [5].

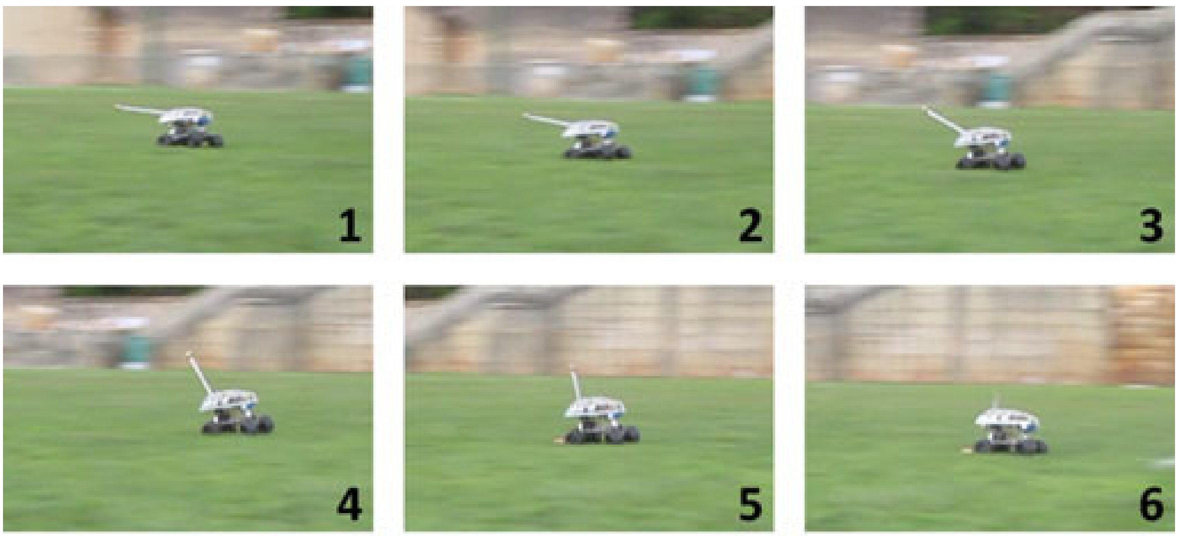

Figure 2.9: Images from [8] showing the robot performing a turn with the tail.

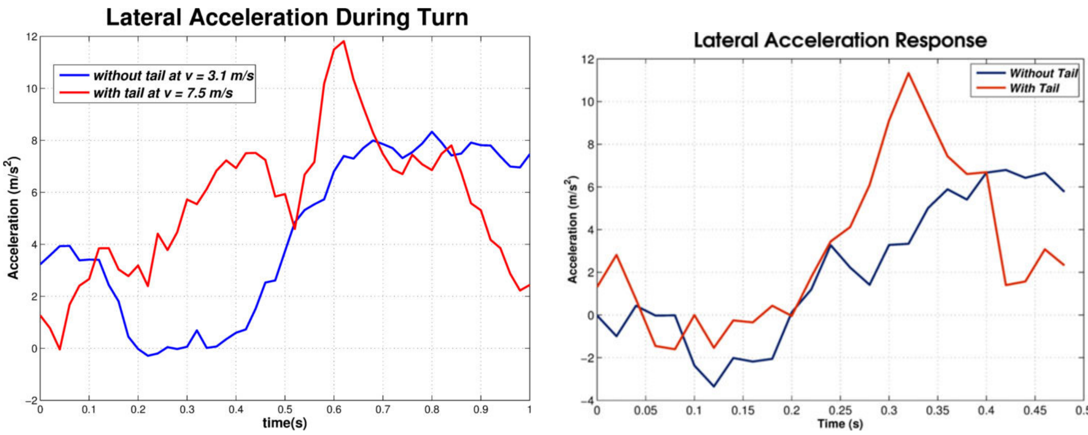

Figure 2.10: Experimental Data from [7] (left) and [8] (right) showing the maximum lateral acceleration achieved with and without and active tail. Note the right graph manages similar results to the left graph.

2.3.2.4 *Terrestrial → Turning → Initiation*

[9], [10] both use similar robot designs, insect like robots that locomote using 6-8 pairs of small legs (in this case [9] used a robot with eight legs, and [10] used six legs) as shown in figure 2.11. Both robots are designed to be very light ($52\,\mathrm{g}$ in [9] and $46\,\mathrm{g}$ in [10]) so the legs have a low friction force with the ground. A suitably weighted tail, when swung out in a horizontal motion, can overcome this friction force and impart enough torque to rotate the body of the robot to a new heading.

[10] compared a open and closed loop response of the tail, while [9] only compared open loop tail responses at different frequencies and amplitudes, as can be seen in figure 2.13.

Both experiments were able to greatly increase the turning rate of the robot over a turn using a differential drive, at $360\,°\,\mathrm{s}^{-1}$ for [10] and $400\,°\,\mathrm{s}^{-1}$ for [9].

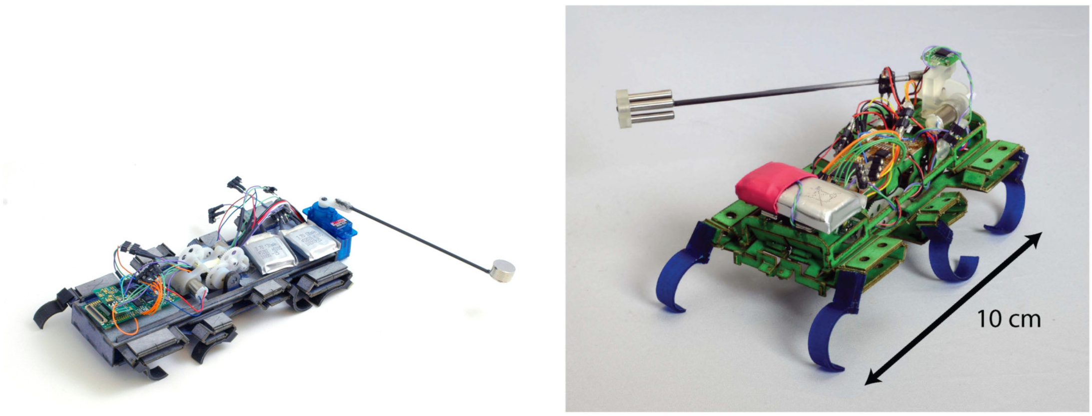

Figure 2.11: Images of the hexapodal and octopodal insect like robots in [9] (left) and [10] (right).

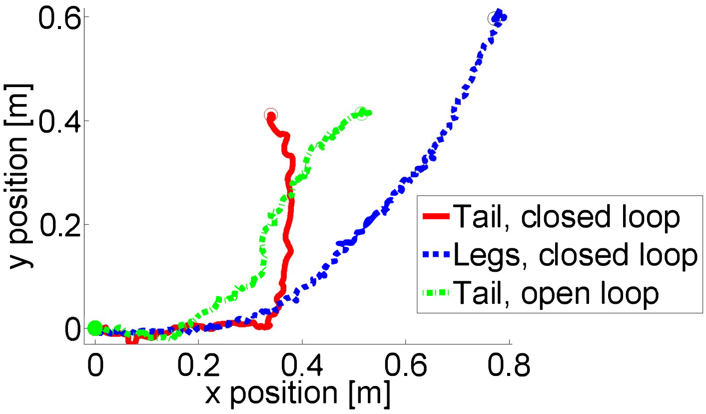

Figure 2.12: Data from [10] comparing the robot path on an XY plane for a 90° differential drive turn, open loop tail turn, and closed loop tail turn. Note the vastly increased sharpness of the turn when a tail is used.

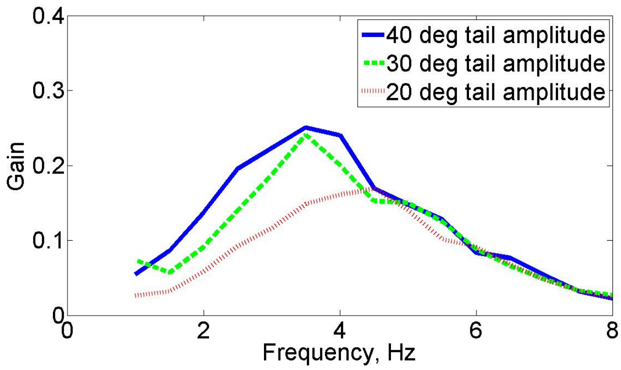

Figure 2.13: Data from [9] showing the gain in yaw rate for various open loop tail trajectories and different frequencies and amplitudes.

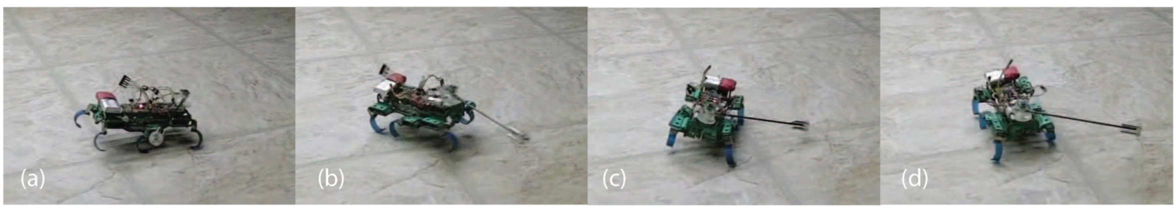

Figure 2.14: Images from [10] showing the robot using its tail to make a turn.

2.3.2.5 *Terrestrial → Balancing → Stability*

The forces that may cause the robot to topple over when balancing can result from both *internal* forces: robot design or joint inertia when moving at high speed, and *external* forces: uneven terrain or impact. [11] is concerned with internal forces, whereas [12] is concerned with external forces.

[11] used a dinosaur like bipedal robot with a long neck and tail. The neck and tail then swung from side to side during the gait, maintaining the stability of the robot. Two experiments were conducted using different strategies for maintaining stability. The "static" method swung the neck and tail in a trapezoidal motion in order to keep the COM within the area of the current foot on the ground. The "dynamic" method calculated the ZMP of the robot and instead constrained that to keep it within the are of the foot. This resulted in a smaller motion of the neck and tail which enabled a faster gait, from $19.5\,\mathrm{mm\,s^{-1}}$ up to a theoretical $208\,\mathrm{mm\,s^{-1}}$, though in practice the velocity was limited by the motor performance.

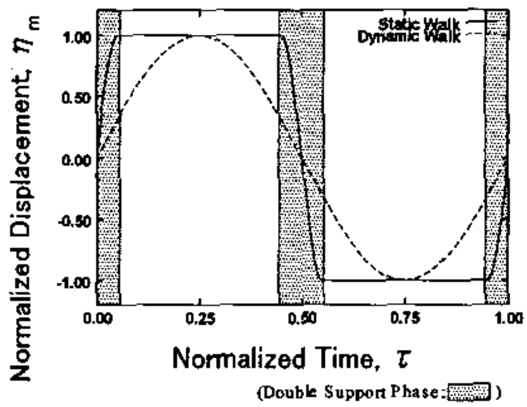

Figure 2.15: Data from [11] showing the normalised change in COM for a static and dynamic walk.

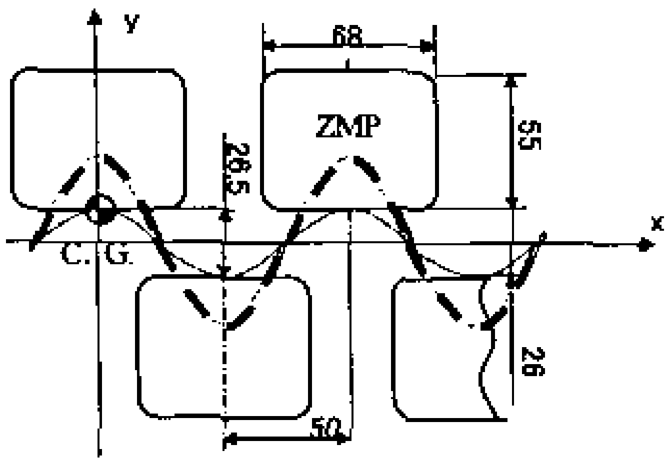

Figure 2.16: Data from [11] showing the trajectory of the COM and ZMP for a static and dynamic walk.

[12] uses a quadrupedal robot closely modelled on a Cheetah which is hit in the torso by a "wrecking ball" to simulate a disturbance. In the control experiment the weighted tail remains static, in the active tail experiment the tail responds in an open loop trajectory when

triggered by an accelerometer that sensed the impact. The active tail experiment was able to significantly reduce the hip displacement after impact, as can be seen in figure 2.18.

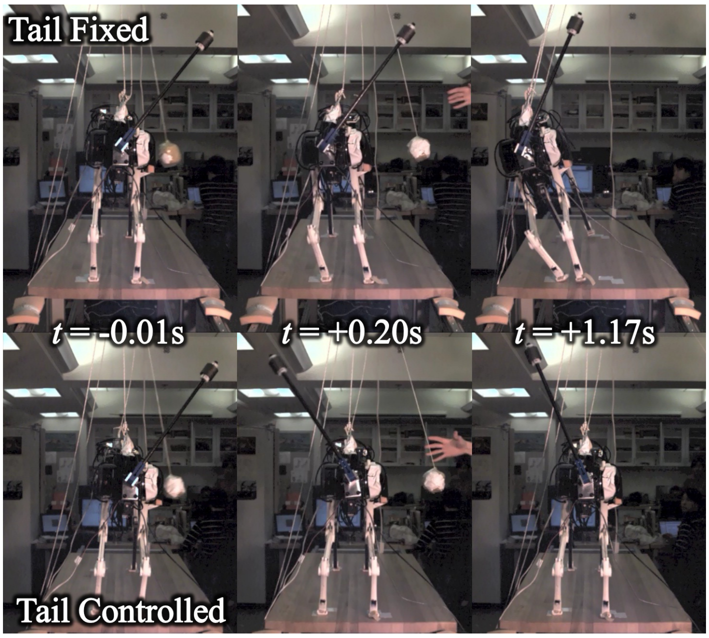

Figure 2.17: Images from [12] showing how the tail or body deflect when hit by the wrecking ball, depending on if the tail is active.

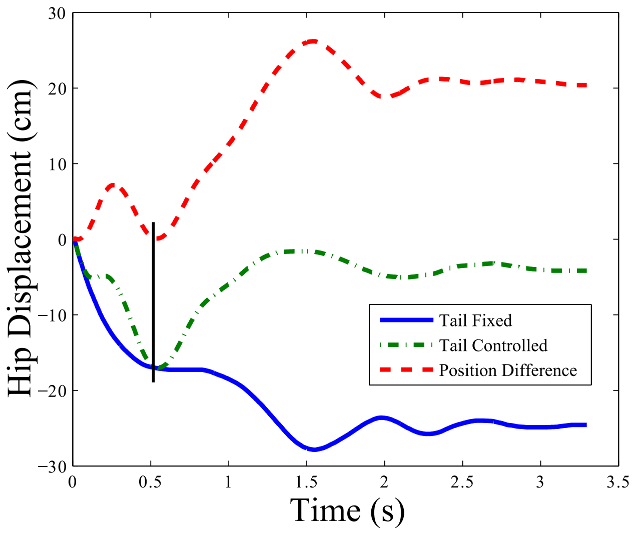

Figure 2.18: Data from [12] showing the difference in hip displacement between a fixed and controlled tail.

2.3.2.6 *Transition → Hopping → Amplification*

[13], [14] both use a tail to increase the magnitude of a hopping gait. [13] increases the *height* of the hop, while [14] increases the *length*.

[13] uses a bipedal robot with a long, flexible tail. The tail consists of six segments, connected together by passive spring revolute joints. The only active joint connects the tail assembly to the robot body. This creates a "whip-like" motion in the tail when the joint is actuated. By experimenting with different spring constants, an optimum value that maximises

jumping height can be found, as can be seen in figure 2.21. Results showed a significant increase in jump height, 256 mm over 240 mm for a model with a rigid tail, and 210 mm for a mode with an inactive tail, demonstrating the superiority of a flexible tail in this application.

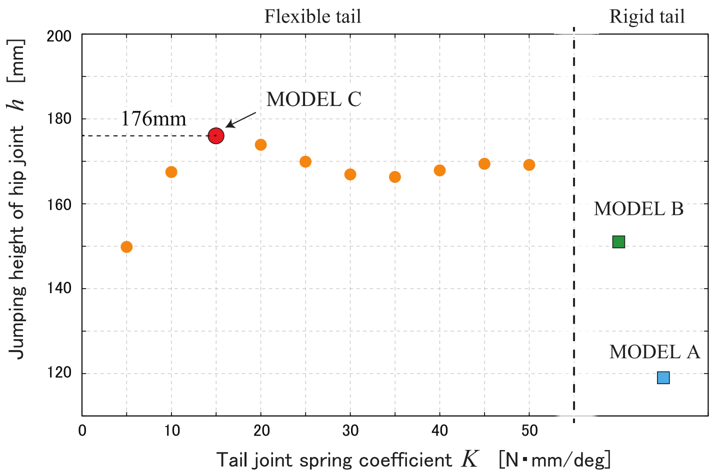

Figure 2.19: Data from [13] showing the optimal spring constant for maximising jumping height.

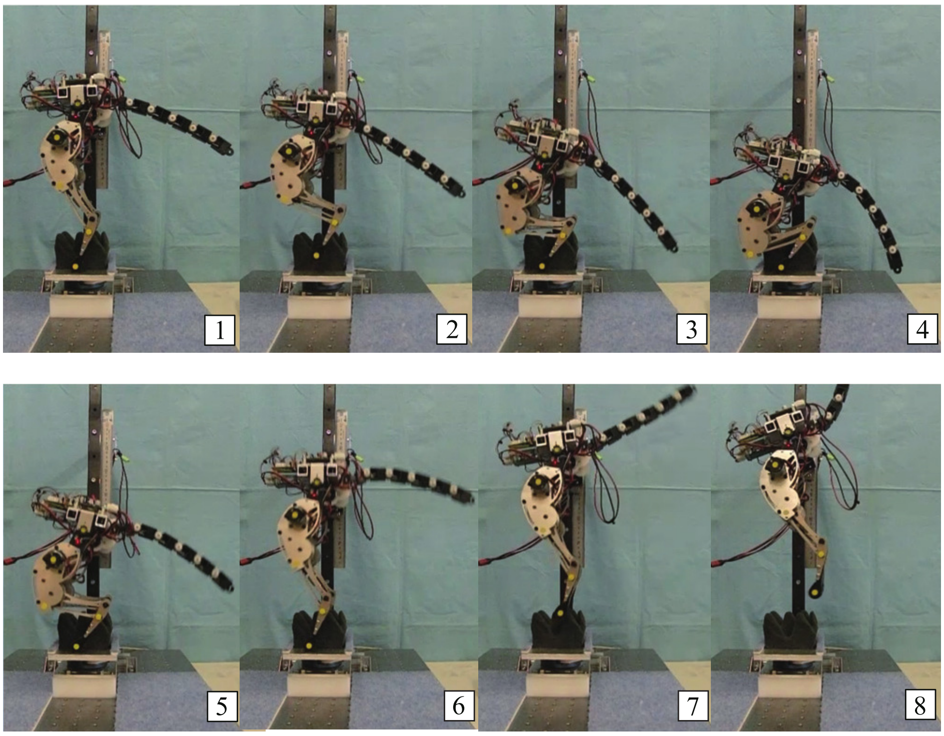

Figure 2.20: Images from [13] showing the motion of the tail during a jump.

[14] uses a quadrupedal robot that locomotes in a galloping motion. By using a weighted tail in an open loop trajectory, the robot is about to increase its forward velocity while also reducing body pitch. Two different tail lengths and masses were used for experiments, a long, light tail (31 g/168 mm), and a short heavy tail (53 g/128 mm). Different open loop amplitudes, $35°$ and $65°$, were also used for each experiment. Results showed an increase in forward velocity and reduction in body pitch, with the best forward velocity of $0.558\,\mathrm{m\,s^{-1}}$ from the short, heavy tail at $35°$, and the best reduction in body pitch per stride of $4.6°$ from the long, light tail at $65°$. These results compared to a forward velocity of $0.479\,\mathrm{m\,s^{-1}}$ and

body pitch per stride of $8.5°$ for a fixed "passive" tail.

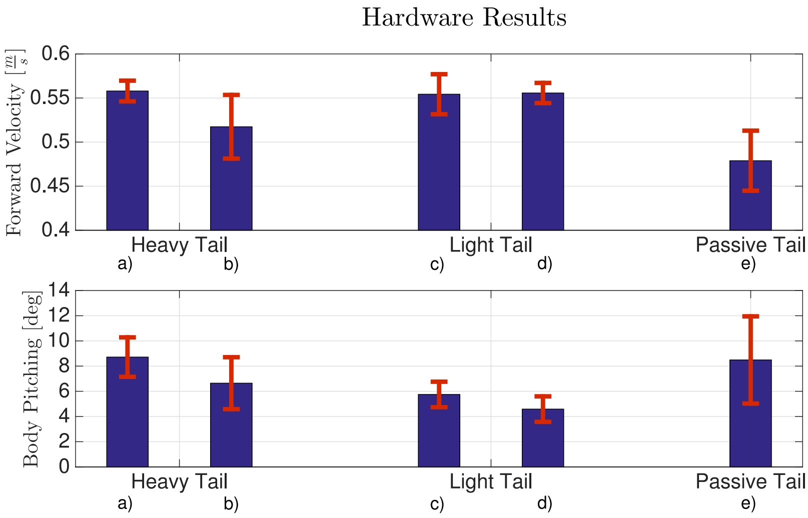

Figure 2.21: Data from [14] showing the increase in forward velocity and/or reduction in body pitch for the different tail lengths and masses. Note that a) and c) correspond to a $35°$ tail amplitude, while b) and d) are a $65°$ amplitude.

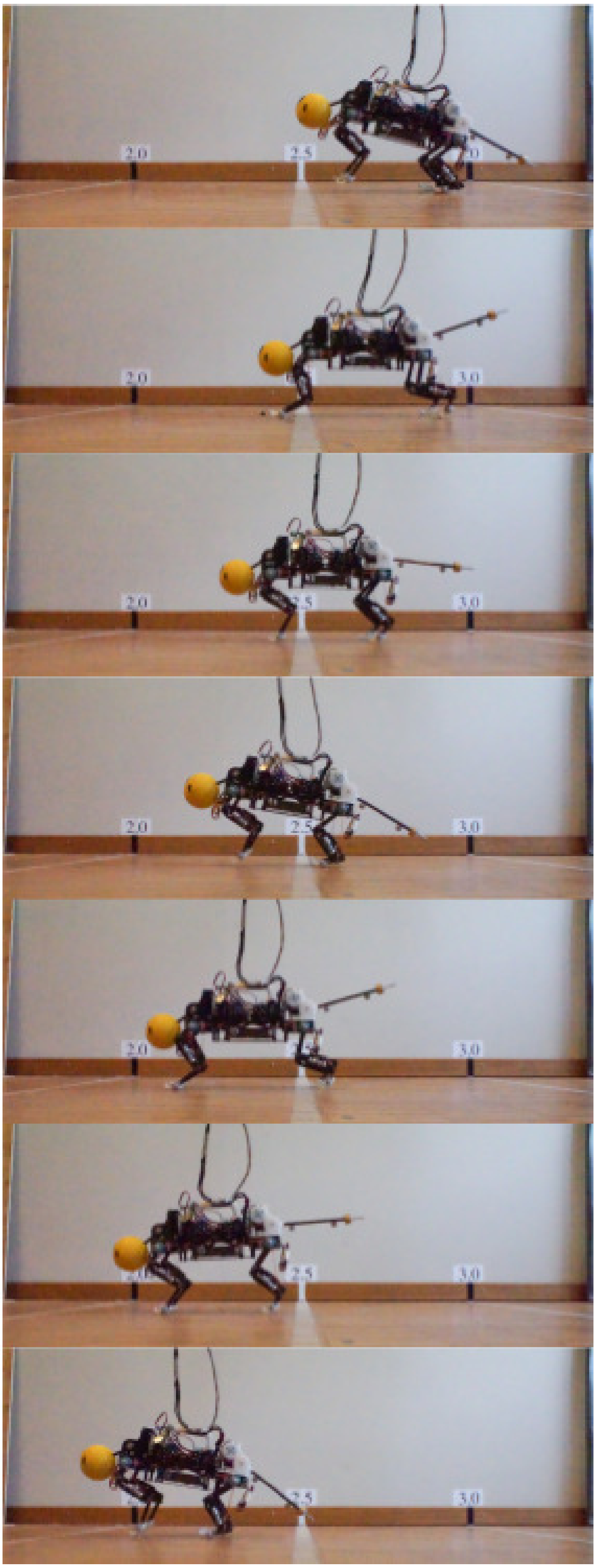

Figure 2.22: Images from [14] showing the motion of the body and tail over a single stride cycle.

2.3.2.7 *Aerial → Hopping → Stability*

[14] also used the tail to reduce body pitch, which prevents the robot from falling over forward when hopping. [15] also used a kangaroo like robot with a tail to also decrease body pitch, in both an open and closed loop tail trajectory. The open loop tail was able to reduce the body pitch range to $5.17°$ and Root Mean Square (RMS) error to $1.17°$, and the closed loop tail to $4.49°$ with an RMS of $0.96°$, as compared to $7.18°$ with an RMS of $2.24°$ for a stationary tail (in this case, *range* refers to the difference between the maximum and minimum pitch angle during the hop).

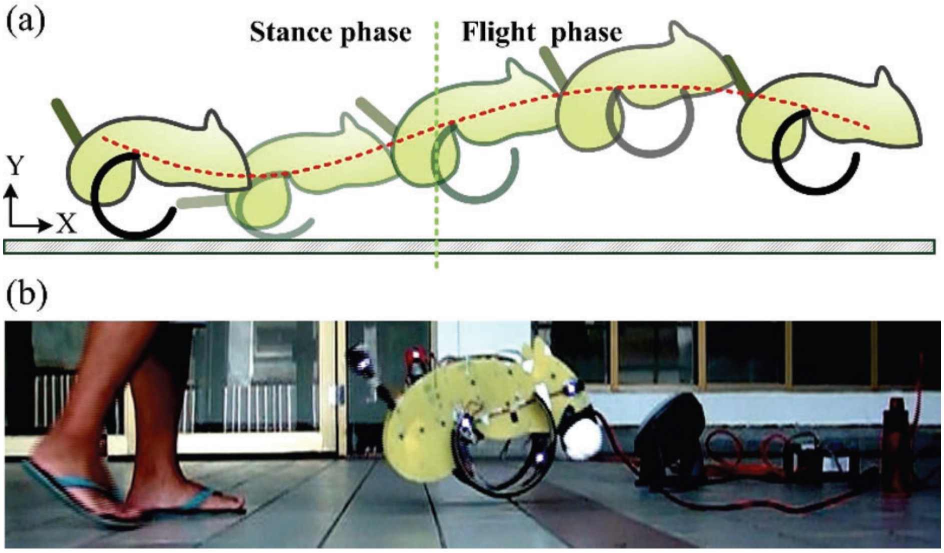

Figure 2.23: Images from [15] showing the a single stride for the robot, and an image of the robot just before landing.

[16] also developed a bipedal robot with a 2 Degrees of Freedom (DOF) tail that was used to maintain a stable hopping motion.

2.3.2.8 *Aerial → Jumping/Falling → Initiation*

[17] uses a wheeled robot with a weighted tail to reorient the robot in mid-air. Two experiments are carried out to this end, where the robot is released from a vertical position on a wall and attempts to land horizontally, and where the robot drives off a ledge and attempts to land on a $45°$ sloped surface. The tail used a Proportional Derivative (PD) feedback controller with body orientation as input. In both experiments, the robot was able to successfully reorient itself.

[18] used a robot that was able to wheel itself to a specific position, then rotate itself using the tail as an appendage into a different orientation which allowed it to launch itself into the air. Then once in the air it would use the tail itself to orient itself back so it landed on its wheels.

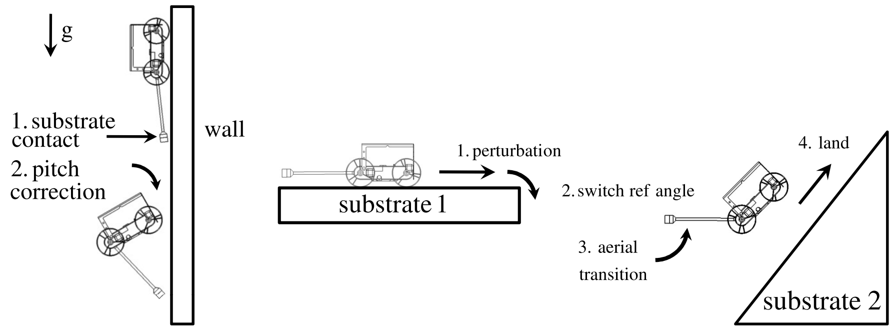

Figure 2.24: Diagrams from [17] outlining the two reorientation experiments.

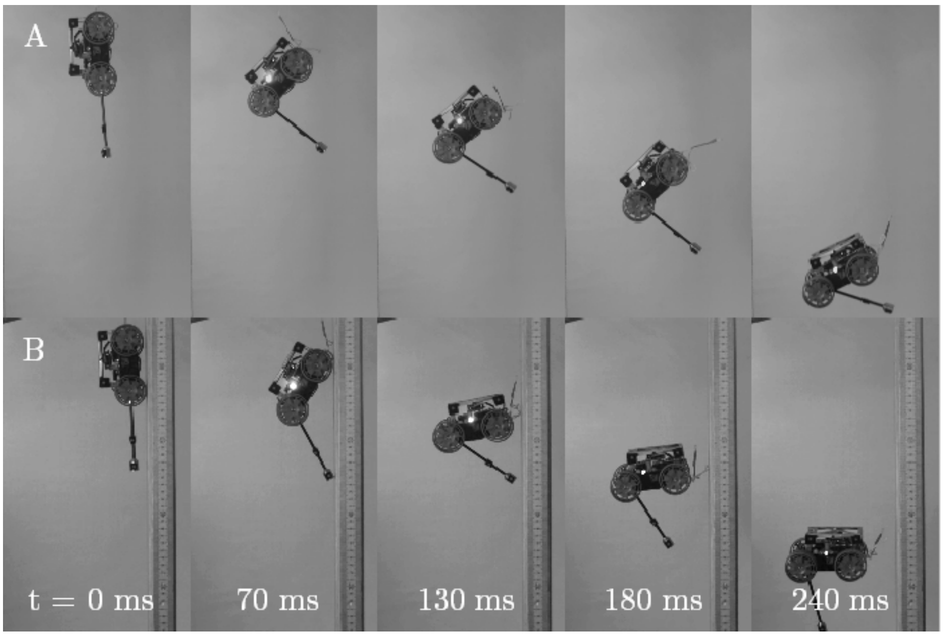

Figure 2.25: Images from [17] showing the wall reorientation experiment.

Figure 2.26: Images from [17] showing the slope reorientation experiment.

2.3.2.9 *Aerial → Jumping/Falling → Stability*

[17] also conducted an experiment where the robot would hit a small obstacle when driving along a surface, causing it to go airborne. Experiments were conducted without a tail, with a static tail, and with a closed loop controlled tail.

[19] had a hexapod robot that was able to remain upright when running off a ledge.

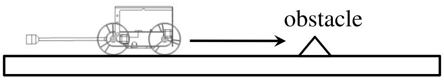

Figure 2.27: Diagram from [17] showing the obstacle impact test.

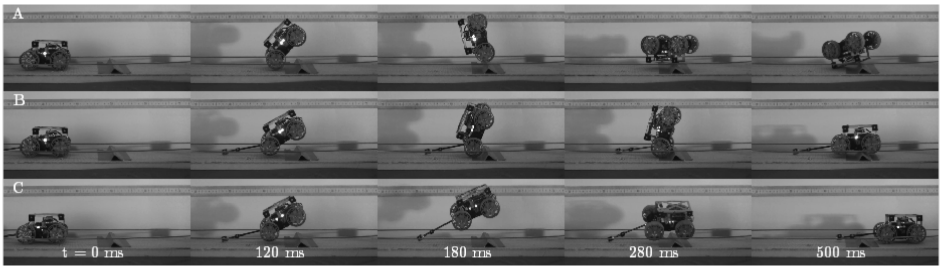

Figure 2.28: Images from [17] showing the slope obstacle impact test without a tail, with a static tail, and with a dynamic tail with closed loop feedback.

2.4 Discussion

Many tails were designed to be multi functional, as evidenced by experiments of different functions within the same publication, and/or multiple publications that included the same robot.

2.4.1 Performance Comparisons in the Selected Publications

A number of experimental publications varied their tail design [13], [14] or control system [15], [18], and were able to record improvements in performance for various metrics. Figure 2.29 shows selected publications performance comparisons, normalised to the best performing variation for each metric, for a unitless comparison. For control systems, the more complex and advanced the better the performance, understandable since a publication is unlikely to test a more complex control system unless there is high confidence in a performance improvement. For tail design, the picture is more complex. While [13] demonstrates a clear improvement in performance for a flexible tail, a more complex design, [14] shows how tail design can result in trade-offs between different metrics, with different tail designs being superior. However, it is possible to see the *Long Light Tail (*$65°$*)* is the optimal choice, since reduction in *Forward Velocity* is slight, but the reduction in *Body Pitch* (a negative metric, where a larger value is worse) is significant, assuming both metrics are equally weighted. Figure 2.29 shows these performance improvements normalised to the best performing configuration at 100%, e.g. a measured result of $[5, 10, 30, 50]$ would be represented as $[10\%, 20\%, 60\%, 100\%]$.

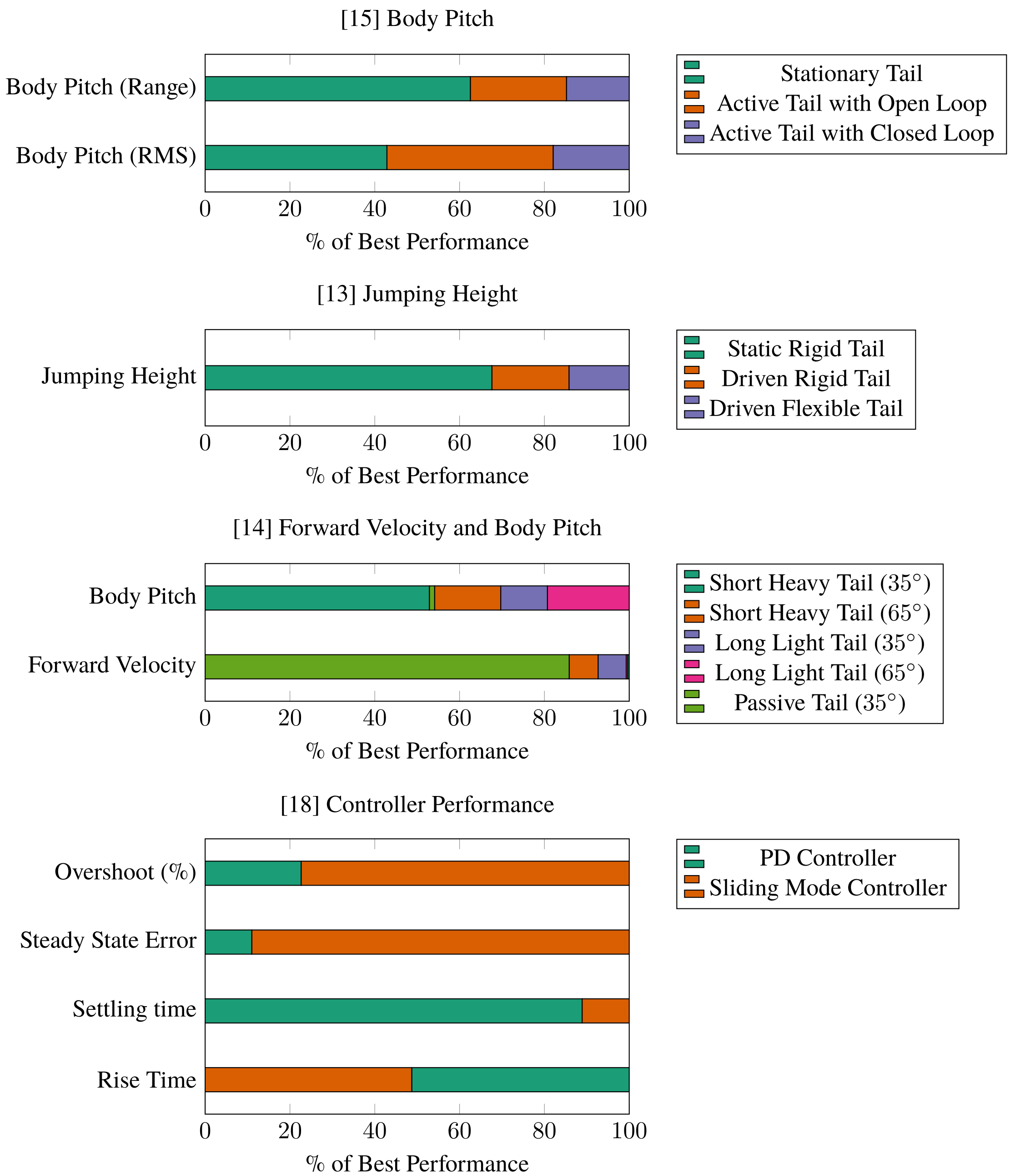

Figure 2.29: Graphs of various publications that varied tail design or control, normalised to the best performing variation (= 100%) for each metric, for a unitless comparison.

2.4.2 Bio-Inspiration

The selected publications contained varying degrees of bio-inspiration, which can be fitted into a hirearchy as shown in figure 2.30. Publications with the least influence mentioned an animal in their research only in a vague fashion, mainly as an introduction to their research, possibly to provide loose justification for their approach. Other publications did take this one step further, and made direct observations on the motion of the animal tail in order to closely approximate them in a robot. For example, [5], [7], [8] all observe the tail motion of a Cheetah when performing certain actions (accelerating, decelerating and turning), and while they do not measure the exact trajectory of those observations, they use a similar motion for their robot tail when the robot is performing the same action. A more intensive approach does take data from an animal performing an action, and compares the data to a

Examination
Publication examines the anatomical structure of part of the animal, and uses this as a basis for a mechanical design element in the robot.

Comparison
Publication takes measurements of the animal in motion, and compares the performance for specific criteria during a given task with the robot.

Observation
Publication sources visual observations on biomechanical motions of the animal, and approximates said motions using the robot.

Inspiration
Publication mentions a particular animal in the introduction, but does not use any data from that animal in the research.

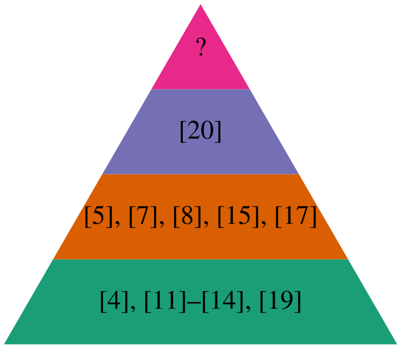

Note: [12] does use *observation* for the simulation, but does not for the experimental work.

Figure 2.30: Hierarchy of bio-inspiration with examples from the selected literature, from least to most influential on the research.

robotic equivalent. For example, [20] makes a direct comparison between the body rotation sensitivity from a perturbation between an Agama Lizard, a robot, and a simulated Velociraptor. What has not been observed in the selected literature is an attempt to to replicate the anatomical structure of an animal tail using mechanical components. This is likely due to a number of reasons, complexity of design and control, redundant actuation, and technological limitations among others. While this approach has been conducted before [21], it has not been seen in the selected literature. This kind of intensive bio-inspiration could be useful in the field of robotic tails in order to explore the potential for performance improvements, and could also help answer questions about why naturally evolved tails are generally more complex and redundant than their robotic counterparts.

2.4.3 Use of Multiple Segment Tails

Only a couple of publications [13], [22] experimented with mobile robots using tails with multiple segments. Other publications [23]–[27] only experimented with multi-segment tails in isolation, some with speculation on future inclusion in a mobile robot. As mentioned in subsections 2.4.1 and 2.3.2.6, [13] managed to achieve a 25 mm improvement in jump height using a sprung flexible tail instead of a rigid one. The relative paucity of experimental multi-segment tails could be explained due to complexities in dynamics and control, as even in [13] only the first joint was actuated and the rest passively spring-loaded, resulting in a simple design and control system. If the future research of some isolated multi-segment tail experiments is realised, then more data will be available.

2.5 Conclusion

Based on the review undertaken here, the field of robotic tails in terrestrial locomotion is very diverse and varied. Tails appear to be used for a number of wide ranging applications in mobile robot locomotion, some with bio-inspiration such as the kangaroo and cheetah for hopping and turning in [8], [15] and some without, such as the addition of a tail to insect like hexapod robots in [9], [10] for inducing steering, which does not occur in nature. The area of aerial dynamics is the most comprehensively researched…There are still several gaps in the research, particularly when it come to experimental studies into multiple segment tails on mobile robots and payload compensation. The former is most likely down to technical limitations, the additional mass and bulk additional actuators is more of an issue on a mobile robot than a static tail or simulation study. There is also the increase in control complexity, which will make stable control of the tail more of a challenge in most of the functions discussed.

By far the most common design for a tail is a rigid single segment with 1-2 DOF, unlike in the animal kingdom where multi-segment tails are the norm. However, a multi-segment approach may still yield advantages, and a simulation study for the primary research application is discussed in chapter **??**.

References

[1] C. C. Kessens and J. Dotterweich, "Ground-based self-righting using inertial appendage methods," in *Unmanned Systems Technology XIX*, International Society for Optics and Photonics, vol. 10195, 2017, p. 1 019 505. DOI: 10.1117/12.2262535.

[2] Y.-H. Kim and D. A. Shell, "Bound to help: Cooperative manipulation of objects via compliant, unactuated tails," *Autonomous Robots*, pp. 1–20, 2018.

[3] B. McInroe, H. C. Astley, C. Gong, *et al.*, "Tail use improves performance on soft substrates in models of early vertebrate land locomotors," *Science*, vol. 353, no. 6295, pp. 154–158, 2016. DOI: 10.1126/science.aaf0984.

[4] Z. Xiuli, G. Jiaqing, and Y. Yanan, "Effects of head and tail as swinging appendages on the dynamic walking performance of a quadruped robot," *Robotica*, vol. 34, no. 12, pp. 2878–2891, 2016. DOI: 10.1017/S0263574716000011.

[5] A. Patel and M. Braae, "Rapid acceleration and braking: Inspirations from the cheetah's tail," in *Robotics and Automation (ICRA), 2014 IEEE International Conference on*, IEEE, 2014, pp. 793–799. DOI: 10.1109/ICRA.2014.6906945.

[6] S. B. Williams, H. Tan, J. R. Usherwood, and A. M. Wilson, "Pitch then power: Limitations to acceleration in quadrupeds," *Biology letters*, vol. 5, no. 5, pp. 610–613, 2009.

[7] A. Patel and M. Braae,
"Rapid turning at high-speed: Inspirations from the cheetah's tail," in *Intelligent Robots and Systems (IROS), 2013 IEEE/RSJ International Conference on*, IEEE, 2013, pp. 5506–5511. DOI: 10.1109/IROS.2013.6697154.

[8] A. Patel and E. Boje, "On the conical motion of a two-degree-of-freedom tail inspired by the cheetah,"
IEEE Transactions on Robotics, vol. 31, no. 6, pp. 1555–1560, 2015.
DOI: 10.1109/TRO.2015.2495004.

[9] A. O. Pullin, N. J. Kohut, D. Zarrouk, and R. S. Fearing,
"Dynamic turning of 13 cm robot comparing tail and differential drive,"
in *Robotics and Automation (ICRA), 2012 IEEE International Conference on*, IEEE, 2012, pp. 5086–5093. DOI: 10.1109/ICRA.2012.6225261.

[10] N. J. Kohut, A. O. Pullin, D. W. Haldane, D. Zarrouk, and R. S. Fearing, "Precise dynamic turning of a 10 cm legged robot on a low friction surface using a tail,"
in *Robotics and Automation (ICRA), 2013 IEEE International Conference on*, IEEE, 2013, pp. 3299–3306. DOI: 10.1109/ICRA.2013.6631037.

[11] K. Takita, T. Katayama, and S. Hirose, "Development of dinosaur-like robot titrus-motion control of the head and tail of miniature robot titrus-iii,"
in *SICE 2002. Proceedings of the 41st SICE Annual Conference*, IEEE, vol. 5, 2002, pp. 2984–2989. DOI: 10.1109/SICE.2002.1195580.

[12] R. Briggs, J.-W. Lee, M. Haberland, and S.-B. Kim,
"Tails in biomimetic design: Analysis, simulation, and experiment," in *Intelligent Robots and Systems (IROS), 2012 IEEE/RSJ International Conference on*, IEEE, 2012, pp. 1473–1480. DOI: 10.1109/IROS.2012.6386240.

[13] R. Sato, S. Hashimoto, A. Ming, and M. Shimojo,
"Development of a flexible tail for legged robot,"
in *Mechatronics and Automation (ICMA), 2016 IEEE International Conference on*, IEEE, 2016, pp. 683–688. DOI: 10.1109/ICMA.2016.7558645.

[14] S. W. Heim, M. Ajallooeian, P. Eckert, M. Vespignani, and A. J. Ijspeert, "On designing an active tail for legged robots: Simplifying control via decoupling of control objectives,"
Industrial Robot: An International Journal, vol. 43, no. 3, pp. 338–346, 2016.
DOI: 10.1108/IR-10-2015-0190.

[15] L. Guan-Horng, L. Hou-Yi, L. Huai-Yu, C. Shao-Tuan, and L. Pei-Chun, "A bio-inspired hopping kangaroo robot with an active tail," *Journal of Bionic Engineering*, vol. 11, no. 4, pp. 541–555, 2014. DOI: 10.1016/S1672-6529(14)60066-4.

[16] J. An, T. Chung, C. H. D. Lo, C. Ma, X. Chu, and K. S. Au, "Development of a bipedal hopping robot with morphable inertial tail for agile locomotion," in *2020 8th IEEE RAS/EMBS International Conference for Biomedical Robotics and Biomechatronics (BioRob)*, IEEE, 2020, pp. 132–139.

[17] E. Chang-Siu, T. Libby, M. Tomizuka, and R. J. Full, "A lizard-inspired active tail enables rapid maneuvers and dynamic stabilization in a terrestrial robot," in *Intelligent Robots and Systems (IROS), 2011 IEEE/RSJ International Conference on*, IEEE, 2011, pp. 1887–1894. DOI: 10.1109/IROS.2011.6094658.

[18] Z. Jianguo, Z. Tianyu, X. Ning, M. W. Mutka, and X. Li, "Msu tailbot: Controlling aerial maneuver of a miniature-tailed jumping robot," *IEEE/ASME Transactions on Mechatronics*, vol. 20, no. 6, pp. 2903–2914, 2015. DOI: 10.1109/TMECH.2015.2411513.

[19] T. Libby, A. M. Johnson, E. Chang-Siu, R. J. Full, and D. E. Koditschek, "Comparative design, scaling, and control of appendages for inertial reorientation," *IEEE Transactions on Robotics*, vol. 32, no. 6, pp. 1380–1398, 2016. DOI: 10.1109/TRO.2016.2597316.

[20] T. Libby, T. Y. Moore, E. Chang-Siu, *et al.*, "Tail-assisted pitch control in lizards, robots and dinosaurs," *Nature*, vol. 481, no. 7380, pp. 181–184, 2012. DOI: doi:10.1038/nature10710.

[21] J. A. Nyakatura, K. Melo, T. Horvat, *et al.*, "Reverse-engineering the locomotion of a stem amniote," *Nature*, vol. 565, no. 7739, pp. 351–355, 2019.

[22] B. Simon, R. Sato, J.-Y. Choley, and A. Ming, "Development of a bio-inspired flexible tail system," in *2018 12th France-Japan and 10th Europe-Asia Congress on Mechatronics*, IEEE, 2018, pp. 230–235.

[23] W. S. Rone, W. Saab, and P. Ben-Tzvi, "Design, modeling, and integration of a flexible universal spatial robotic tail," *Journal of Mechanisms and Robotics*, vol. 10, no. 4, p. 041 001, 2018.

[24] W. Saab, W. S. Rone, and P. Ben-Tzvi, "Discrete modular serpentine robotic tail: Design, analysis and experimentation," *Robotica*, pp. 1–25, 2018.

[25] W. Saab, J. Yang, and P. Ben-Tzvi, “Modeling and control of an articulated tail for maneuvering a reduced degree of freedom legged robot,” in *2018 IEEE/RSJ International Conference on Intelligent Robots and Systems (IROS)*, IEEE, 2018, pp. 2695–2700.

[26] W. S. Rone and P. Ben-Tzvi, “Continuum robotic tail loading analysis for mobile robot stabilization and maneuvering,” in *ASME 2014 International Design Engineering Technical Conferences & Computers and Information in Engineering Conference IDETC/CIE 2014*, American Society of Mechanical Engineers, 2014. DOI: 10.1115/DETC2014-34678.

[27] Y. Liu, J. Wang, and P. Ben-Tzvi, “A cable length invariant robotic tail using a circular shape universal joint mechanism,” *Journal of Mechanisms and Robotics*, vol. 11, no. 5, 2019.

Chapter 3

Creating a Configurable Payload for Instability Experiments

In this chapter, an abstract mathematical model of the configurable payload is conceived, which the mass and COM of a specific permutation of the payload can be derived from. Then three separate sets of "test points" are considered to cover a wide range of the available configuration space within the chosen robot arms performance limits, using a combined mass and COM vector as a target which finds the closest permutation using a search function, or extrema which maps onto a specific permutation. For target test points, two search methods are examined, one brute force method for small permutation sets and one for larger sets where a brute force method would be computationally intractable. Then the chosen implementation is described, including the number of block materials, the number of blocks, the size and design of the container and the chosen search method. The results of this implementation for all test point sets are then tabulated and graphed. In the discussion, the limitations of the mass and COM range are considered, and potential designs to expand the range and scope of the experiments in chapter **??** *are conceived, specifically improving the range of the COM and simulating dynamic loads.*

3.1 Introduction

In order to generate a diverse set of test data for the experiments in chapter 4, a configurable payload was conceived, an object that could be configured to have a wide range of masses and COM. A series of test points can then be generated which have a specific mass and COM, and a matching algorithm can be used to find the configuration that mostly closely matches these parameters. The experiments can then be run with each of these test points to generate the test data.

The payload consists of a matrix of cubes of various materials packed tightly into a Three Dimensional (3D) printed container. The cubes are designed to be changed after each experimental run to alter the mass and COM of the payload. A lid on the container prevents the cubes from falling out during the experiment, and the exterior design of the box may accommodate additional features to improving the handling of the payload by the robot arm.

The test points can then be generated by considering the *Configuration Space* of the payload design, i.e. how many permutations can be generated given a $n \times n \times n$ matrix of cubes, where each cube can be a number of different materials. The mass and COM can then be calculated for each permutation, taking into taking into account the material density and mass and COM of the container. "Extrema" test points can then be found simply by finding the permutation with the maximum or minimum mass and COM, or combination thereof. Depending on the number of permutations, a search method can then be used that accepts an arbitrary mass and COM as a target, and finds the nearest permutation to that target for other test point sets.

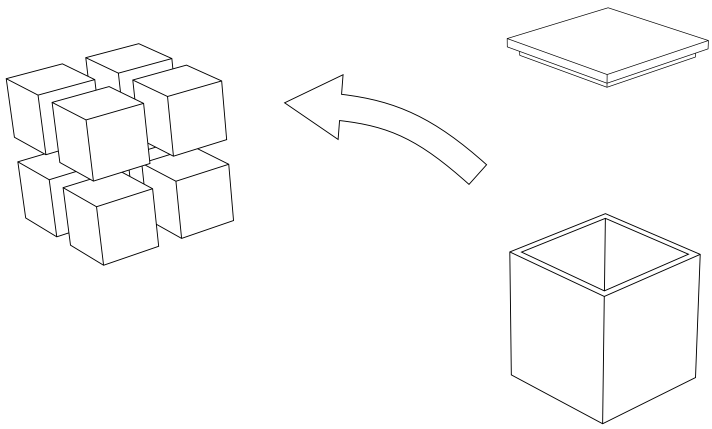

Figure 3.1: Concept drawing of the configurable payload.

3.2 Mathematical Design

3.2.1 Configuration Space

Firstly, consider a positive real set of material densities $\mathcal{P} \in \mathbb{R}^{+}$, each element the density (in $\mathrm{kg\,m^{-3}}$) of a material to be used:

$$\mathcal{P} = \{\rho_1, \rho_2 \ldots \rho_n \mid \rho_i > 0\} \tag{3.1}$$

Each permutation can then be defined as an $n \times n \times n$ matrix $\boldsymbol{C}$, such that each element is an element of $\mathcal{P}$, where n^3 is the number of cubes in the matrix:

$$\boldsymbol{C} = (c_{ijk}) \in \mathbb{R}^{n^n} \mid (c_{ijk}) \in \mathcal{P} \tag{3.2}$$

$\mathcal{Z}$ can then be defined as the set of all permutations of $\boldsymbol{C}$.

To calculate the mass of the permutation, take the sum of all the cube densities multiplied by their volume a^3, where a is the cube edge length, plus the container mass m_c:

$$M(\boldsymbol{C}) = \left(\sum_{i=1}^{n}\sum_{j=1}^{n}\sum_{k=1}^{n} c_{ijk}a^3\right) + m_c \tag{3.3}$$

To calculate the COM, take the sum of each cube mass multiplied by its position relative to the centroid of the center cube (c_{222}), which can be calculated from the cube indexes ijk, plus the container COM $\boldsymbol{r}_c$ if non-zero:

$$R(\boldsymbol{C}) = \frac{\left(\sum_{i=1}^{n}\sum_{j=1}^{n}\sum_{k=1}^{n} c_{ijk}a^4\left(\begin{bmatrix} i & j & k \end{bmatrix} - n + 1\right)\right) + \boldsymbol{r}_c}{M(\boldsymbol{C})} \tag{3.4}$$

The *configuration space* $\mathcal{Y}$ can then be considered as a set of $\mathbb{R}^4$ vectors containing the target mass and COM concatenated as $\begin{bmatrix} m_i & \boldsymbol{r}_i \end{bmatrix}$ of each element. As such, $\mathcal{Y}$ is a codomain of $\mathcal{X}$, such that $H : \mathcal{X} \mapsto \mathcal{Y}$ where map function H is $\begin{bmatrix} M(\boldsymbol{C}) & R(\boldsymbol{C}) \end{bmatrix}$

3.2.2 Test Point Sets

Test points can either be derived from subsets of $\mathcal{X}$ defined by logical expressions, or the nearest neighbours of $\mathcal{Y}$ from a target mass and COM concatenated into a vector as in H, found by a *search method* (see subsection **??**).

3.2.2.1 Extrema Set ($\mathcal{E}$)

The extrema set is designed to test the extremas of the space of $\mathcal{Z}$ for both $M(\mathcal{Z})$ and $R(\mathcal{Z})$. The extrema set if defined from a set of logical constraints. The first two constraints of the set find the maximum and minimum values of the payload mass using $M(\mathcal{Z})$, and the next four constraints use the payload COM using $M(\mathcal{C})$ to get the maximum and minimum values of the x and y component of the COM. Finally, the last four constraints define the diagonal maximum and minimum values where the COM components match $x = y$ or $x = -y$.

$$\mathcal{E} = \left\{ \boldsymbol{x} \subset \mathcal{Z} \mid \begin{cases} M(\boldsymbol{x}) = \text{max}\,\{M(\mathcal{Z})\} \\ M(\boldsymbol{x}) = \text{min}\,\{M(\mathcal{Z})\} \\ R(\boldsymbol{x})_x = \text{max}\,\{R(\mathcal{Z})_x\} \\ R(\boldsymbol{x})_x = \text{min}\,\{R(\mathcal{Z})_x\} \\ R(\boldsymbol{x})_y = \text{max}\,\{R(\mathcal{Z})_y\} \\ R(\boldsymbol{x})_y = \text{min}\,\{R(\mathcal{Z})_y\} \\ R(\boldsymbol{x})_x = \text{max}\,\{R(\mathcal{Z})_x\} \wedge R(\boldsymbol{x})_x = R(\boldsymbol{x})_y \\ R(\boldsymbol{x})_x = \text{min}\,\{R(\mathcal{Z})_x\} \wedge R(\boldsymbol{x})_x = R(\boldsymbol{x})_y \\ R(\boldsymbol{x})_x = \text{max}\,\{R(\mathcal{Z})_x\} \wedge R(\boldsymbol{x})_x = -R(\boldsymbol{x})_y \\ R(\boldsymbol{x})_x = \text{min}\,\{R(\mathcal{Z})_x\} \wedge R(\boldsymbol{x})_x = -R(\boldsymbol{x})_y \end{cases} \right\} \tag{3.5}$$

Mass Limited $\mathcal{E}$ When this set was generated, it was found that $M\left(\mathcal{E}_1\right)$ was greater than the chosen robot arm in chapter **??** could safely lift ($2.0\,\mathrm{kg}$ [1]). Experiment trials also found the grippers were failing to consistently hold masses lower than this for long enough to complete the experiment. Therefore, $M(\boldsymbol{x}) = \text{max}\,\{M(\mathcal{Z})\}$ in $\mathcal{E}$ was changed to $\begin{bmatrix} m_{max} & 0 & 0 & 0 \end{bmatrix}$ where m_{max} is the mass limit that the robot arm can lift reliably. One of the search methods described in section **??** can then be used to find the nearest point in configuration space.

3.2.2.2 Cube Set ($\mathcal{C}$)

The cube set is defined by the vertices of a cube of size b centred around the COM origin $\begin{bmatrix} 0 & 0 & 0 \end{bmatrix}$.

$$\mathcal{C} = \left\{ \boldsymbol{x} \subset \mathcal{C} \mid \begin{bmatrix} \pm\frac{b}{2} & \pm\frac{b}{2} & \pm\frac{b}{2} \end{bmatrix} = \boldsymbol{x} \right\} \tag{3.6}$$

3.2.2.3 Balanced Set ($\mathcal{B}$)

The balanced set is defined by q points in $\mathcal{C}$ subject to the constraint $R(\boldsymbol{x})_x = 0 \wedge R(\boldsymbol{x})_y = 0$. This can be defined as a "balanced" set as the COM x and y components are both zero. The points are evenly spaced between the maximum and minimum mass as defined in section **??**.

$$\begin{aligned} m_r &= \frac{\text{max}\{M(\mathcal{Z})\} - \text{min}\{M(\mathcal{Z})\}}{q+1} \\ \boldsymbol{z} &= \begin{bmatrix} m_r & 2m_r & \cdots & qm_r \end{bmatrix} \\ \mathcal{B} &= \{\boldsymbol{x} \subset \mathcal{C} \mid z_i = \boldsymbol{x} \wedge R(\boldsymbol{x})_x = 0 \wedge R(\boldsymbol{x})_y = 0\} \end{aligned} \tag{3.7}$$

3.2.3 Search Methods

When considering a viable search method given a target, the cardinality of $\mathcal{X}$ is important to consider. It is defined as $|\mathcal{X}| = |\mathcal{P}|^{n^3}$ which increases super exponentially with n. For example, when $|\mathcal{P}| = 4$, $n = 2$ results in 65536 permutations and $n = 3$ results in approximately 1.8×10^{16} permutations. It's very clear that when $n > 2$ for non-trivial cardinalities of $\mathcal{P}$, any kind of brute-force method is not computationally tractable. Therefore, a brute-force nearest neighbour method (see subsection 3.2.3.2) would be suitable for when $n = 2$, and a heuristic search method such as simulated annealing (see subsection 3.2.3.1) method would be suitable for when $n > 2$.

3.2.3.1 Multiobjective Simulated Annealing

Simulated annealing [2] is a modification to a gradient descent optimisation that allows the algorithm the chance to "jump out" of local minima early on (even though the approximation becomes temporarily worse). However, as the number of remaining steps decreases, that probability becomes smaller, becoming more and more like gradient descent. First, like any gradient descent algorithm, two things need to be generated, the initial configuration $\boldsymbol{C_0}$, which can be random or manually selected, and the function $\mathcal{N}(\boldsymbol{C})$ which creates a set of all the "neighbours" of $\boldsymbol{C}$. In this case, this can be defined as the subset of $\mathcal{X}$ where the difference between $\boldsymbol{C}$ and an element of $\mathcal{N}(\boldsymbol{C})$ is one and only one $c_{ijk} \neq c_{ijk}$:

$$\mathcal{N}(\boldsymbol{C}) = \{x \subset \mathcal{X} \mid \exists! \left(x_{ijk} \neq c_{ijk}\right)\} \tag{3.8}$$

Then the simulated annealing function can be described as follows:

1. Set $\boldsymbol{C}$ to the initial permutation $\boldsymbol{C_0}$.
2. For each of the optimisation steps:
   (a) Set the temperature value t with function $T\left(\frac{k_{max}}{k}\right)$ which takes into account the number of remaining steps.
   (b) Set $\boldsymbol{C}_{new}$ as a random element from the set of all neighbours of $\boldsymbol{C}$ as defined by $\mathcal{N}(\boldsymbol{C})$.
   (c) Use acceptance probability function $P\left(E(\boldsymbol{C}), E(\boldsymbol{C}_{new}), t\right)$ where $E(\boldsymbol{C})$ is the energy function.
   (d) Compare that value with a random uniformly distributed real number between 0 and 1. If greater than or equal to, then replace $\boldsymbol{C}$ with $\boldsymbol{C}_{new}$. Otherwise, keep it the same.
   (e) Repeat with $\boldsymbol{C}$ until there are no remaining steps.

3. Return the approximated permutation $\boldsymbol{C}$.

$\boldsymbol{C} = \boldsymbol{C}_0$
for $k \leftarrow 1, k_{max}$ **do**
  $t = T\left(\frac{k_{max}}{k}\right)$
  $\boldsymbol{C}_{new} = \mathcal{N}(\boldsymbol{C}) \xleftarrow{R} x$
  if $P(E(\boldsymbol{C}), E(\boldsymbol{C}_{new}), t) \geq x \sim U([0,1])$ **then**
    $\boldsymbol{C} = \boldsymbol{C}_{new}$
  end if
end for
return $\boldsymbol{C}$

Energy Function Simulated annealing can also be adapted for multi-objective optimisation [3], so it is possible to generate test points that approximate a desired mass and COM simultaneously.

Cooling Function The function which controls the probability of exiting local minima (known as the *temperature*) is known as the *cooling function*. This function can be any function which monotonically decreases (except in adaptive simulated annealing where it is dependant on the accuracy of the current approximation). Different functions will result in a different cooling profile, generally decreasing quickly in the first few steps, and then slowing down after that.

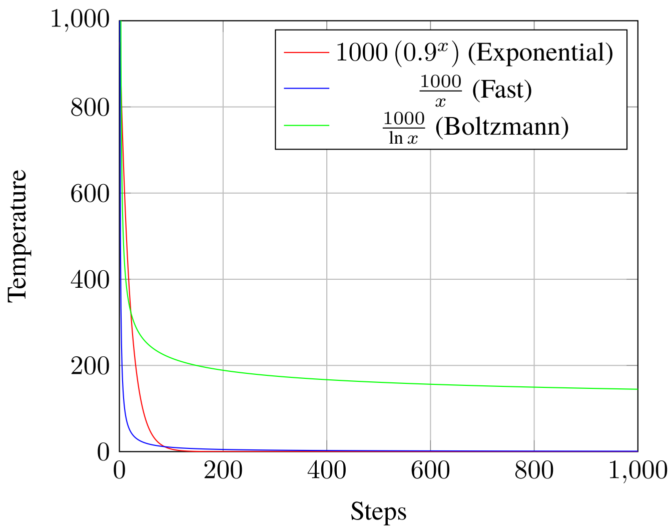

Figure 3.2: Various temperature cooling profiles for simulated annealing, assuming 1000 steps.

3.2.3.2 Nearest Neighbour

If $\mathcal{X}$ is suitably small, then a brute-force method can be used which is guaranteed to find the nearest element to the target within a finite time. This can be done by calculating the L2 norms between the target vector t and all the elements of $\mathcal{Y}$ and finding the minimum. If there are several elements in the domain of $\mathcal{X}$, then one is chosen at random from this set.

$$NN(t, \mathcal{X}) = \min \{ \|t - x\|_2 \mid \forall x \in \mathcal{Z} \} \tag{3.9}$$

3.3 Implementation

3.3.1 Container Design

The internal width of the container was chosen to be 76 mm, which combined with a wall width of 5 mm gives an overall width of 81 mm. Therefore, each cube would be $\frac{75}{n}$mm in size, to allow for fitting clearance. For additional resiliency, the base would be an additional 4 mm, giving the container an overall height of 90 mm with the lid (not including gripper guides). A dimensioned schematic is shown in figure 3.3.

Two sides of the container were made of a textured pattern designed to enhance grip when picked up by the robot arm. The other two sides had small viewports centred around each cube, for permutation verification during the experiments in chapter 4. The lid of the container had a small notch to allow for it to be levered off in case of a tight fit, and guides to ensure the robot arm grippers would pick up the container in the same location each time, ensuring experiment repeatability. A labelled photograph is shown in figure 3.4.

The cube was 3D printed in Polylactic Acid (PLA) with an 80% fill density. This gave it a total mass of 0.221 kg which provides the value for m_c. By design, the COM of the container would be 0 mm in both the x and y direction, to within a reasonable manufacturing tolerance. Due to the minimal contribution of the container to the total mass, this was a suitable assumption.

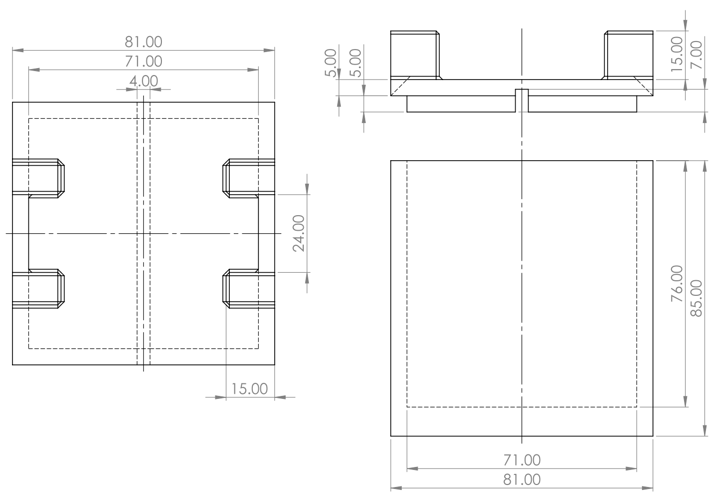

Figure 3.3: Schematic of the container, including body and lid.

3.3.2 Selected Search Method

Initially an $n = 3$ configuration was used with the acceptance probability function *Rule M* from [3]. This is a weighted blend of two other algorithms defined in the paper, *Rule P* and

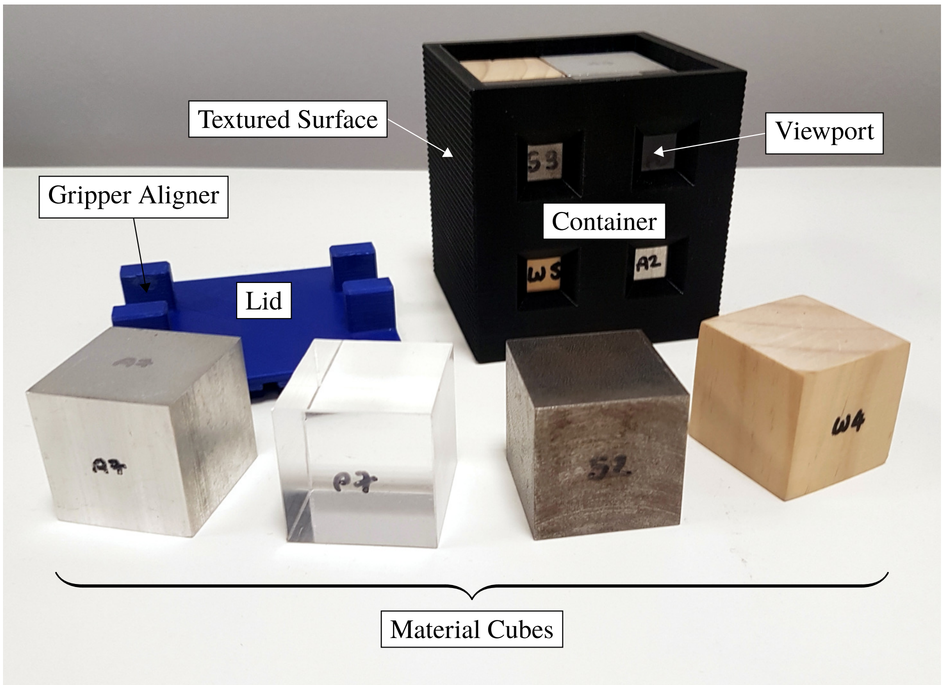

Figure 3.4: Labelled photograph of the final container design, along with the material cubes.

Rule W with a weighting coefficient $\alpha \in (0,1) \subset \mathbb{R}$. There is also a weighting vector for each element of the test point $\boldsymbol{w} \in \mathbb{R}^4 \mid w_i \in (0,1)$.

$$P(\boldsymbol{x}, \boldsymbol{y}, \boldsymbol{w}, t) = \alpha \underbrace{\prod_{i=1}^{m} \min\left\{1, e^{\frac{w_i(x_i - y_i)}{t}}\right\}}_{\text{Rule P}} + (1-\alpha) \underbrace{\min\left\{1, \max_{i=1,\ldots,m}\left\{1, e^{\frac{w_i(x_i-y_i)}{t}}\right\}\right\}}_{\text{Rule W}} \tag{3.10}$$

Unfortunately it was difficult to find a stable and consistent result even after a long time running the algorithm.

Therefore as an alternative, the $n = 2$ configuration was used, with larger cubes to compensate.

3.3.3 Material Selection

In order to produce a reasonably wide and dense configuration space, four materials: *wood*, *plastic*, *aluminium* and *steel*, were chosen. More dense materials, such as nickel and lead, were rejected due to difficulty sourcing stock of the correct size, or issues with machining. Initially estimated densities were used in order to test the simulated annealing algorithm, but after the cubes were manufactured, it was possible to get an average density based on the measured mass of each cube as seen in figure 3.6, given a cube size of $35\,\text{mm}$. Table 3.1 lists the exact kind of material used, and its calculated density. These differ from many stated values available from other sources such as online material databases, likely de to small discrepancies in cube size due to manufacturing tolerances and variability in material

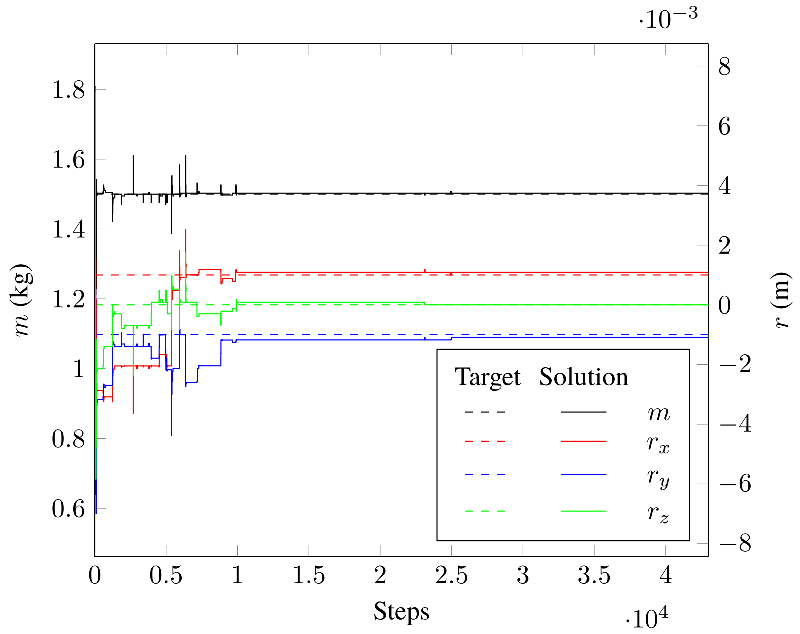

Figure 3.5: Simulated annealing output for the target $[1.5 \quad 0.001 \quad 0.001 \quad 0.001]$ with $\alpha = 0.997$ and even weighting $w_m, \boldsymbol{w_r} = 0.25$ for 4.3×10^4 steps.

composition (particularly for wood since the blocks required sanding in order to fit in the container, and due to the less precise properties of natural materials).

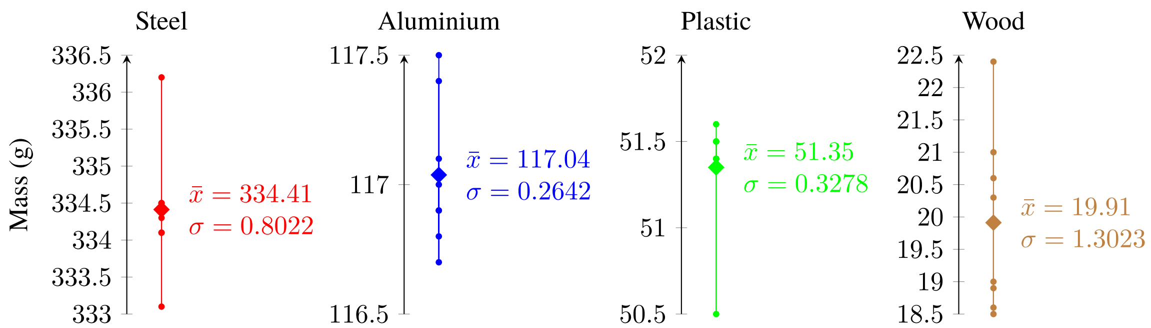

Figure 3.6: Masses for each set of eight 35 mm cubes of the configurable payload for each of the four materials, with the mean mass $\bar{x}$ and standard deviation σ of each set.

Material	Variant	Density (kg m^{-3})
Wood	Pine	464.37
Plastic	Acrylic	1201.9
Aluminium	6082	2740
Steel	EN3B	7800

Table 3.1: The materials chosen for the cubes.

3.4 Results

3.4.1 Configuration Space

Given a $2 \times 2 \times 2$ matrix of cubes with the materials in table 3.1, there were a total of 65536 permutations, with a total mass range of $[0.38, 2.90]$kg, and a total COM range of $[-13.44, 13.44]$mm on all axes. As some permutations mapped to the same point in configuration space, there were 62969 unique mass and COM vectors.

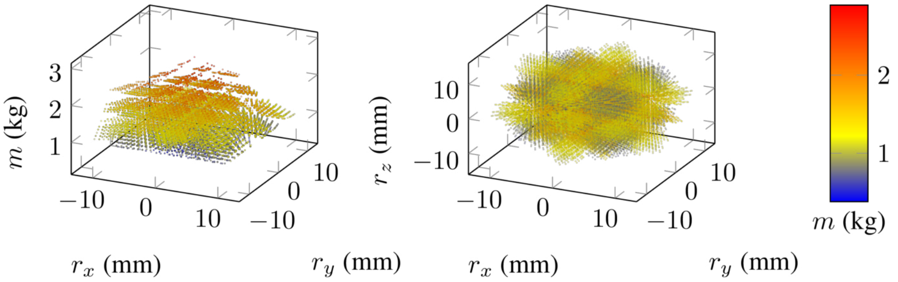

Figure 3.7: Scatter graph of all 62969 unique mass and COM vectors.

3.4.2 Test Points

The mass limit m_{max} for the extrema set was set at 1.25 kg, and the cube set length parameter b was set at 7 mm.

3.4.2.1 Mass and COM

m	$\boldsymbol{r}$
	Extrema Set ($\mathcal{E}$)
1.204	$\begin{bmatrix} 0.012 & 0.000 & -0.000 \end{bmatrix}$
1.204	$\begin{bmatrix} 0.000 & 0.012 & -0.000 \end{bmatrix}$
1.204	$\begin{bmatrix} -0.012 & 0.000 & -0.000 \end{bmatrix}$
1.204	$\begin{bmatrix} 0.000 & -0.012 & -0.000 \end{bmatrix}$
0.380	$\begin{bmatrix} 0.000 & 0.000 & 0.000 \end{bmatrix}$
1.009	$\begin{bmatrix} 0.011 & 0.011 & -0.000 \end{bmatrix}$
1.009	$\begin{bmatrix} -0.011 & -0.011 & 0.000 \end{bmatrix}$
1.009	$\begin{bmatrix} 0.011 & -0.011 & 0.000 \end{bmatrix}$
1.009	$\begin{bmatrix} -0.011 & 0.011 & 0.000 \end{bmatrix}$

Table 3.2: Table of the vectors of $\mathcal{E}$, excluding the mass-limited element.

3.4.2.2 Material Permutations

Target m	Target $\boldsymbol{r}$	Nearest m	Nearest $\boldsymbol{r}$	L2 Norm Error
Extrema Set ($\mathcal{E}$)				
1.250	$[0.000 \quad 0.000 \quad *]$	1.204	$[0.000 \quad 0.000 \quad -0.009]$	4.556×10^{-2}
Cube Set ($\mathcal{C}$)				
$*$	$[-0.007 \quad -0.007 \quad -0.007]$	0.987	$[-0.007 \quad -0.007 \quad -0.007]$	5.244×10^{-4}
$*$	$[-0.007 \quad -0.007 \quad 0.007]$	0.987	$[-0.007 \quad 0.007 \quad -0.007]$	2.023×10^{-2}
$*$	$[-0.007 \quad 0.007 \quad -0.007]$	0.987	$[0.007 \quad -0.007 \quad -0.007]$	2.023×10^{-2}
$*$	$[-0.007 \quad 0.007 \quad 0.007]$	0.987	$[0.007 \quad 0.007 \quad -0.007]$	2.023×10^{-2}
$*$	$[0.007 \quad -0.007 \quad -0.007]$	0.987	$[-0.007 \quad -0.007 \quad 0.007]$	2.023×10^{-2}
$*$	$[0.007 \quad -0.007 \quad 0.007]$	0.987	$[-0.007 \quad 0.007 \quad 0.007]$	2.023×10^{-2}
$*$	$[0.007 \quad 0.007 \quad -0.007]$	0.987	$[0.007 \quad -0.007 \quad 0.007]$	2.023×10^{-2}
$*$	$[0.007 \quad 0.007 \quad 0.007]$	0.987	$[0.007 \quad 0.007 \quad 0.007]$	5.244×10^{-4}
Balanced Set ($\mathcal{B}$)				
0.598	$[0.000 \quad 0.000 \quad *]$	0.575	$[0.000 \quad 0.000 \quad 0.000]$	2.229×10^{-2}
0.815	$[0.000 \quad 0.000 \quad *]$	0.771	$[0.000 \quad 0.000 \quad -0.004]$	4.459×10^{-2}
1.033	$[0.000 \quad 0.000 \quad *]$	0.966	$[0.000 \quad 0.000 \quad 0.000]$	6.688×10^{-2}

Table 3.3: Table of the target and actual vectors for $\mathcal{C}$, $\mathcal{B}$ and the mass limited element of $\mathcal{E}$ with the L2 norm error. $*$ notation indicates "don't care" and is excluded from the search algorithm.

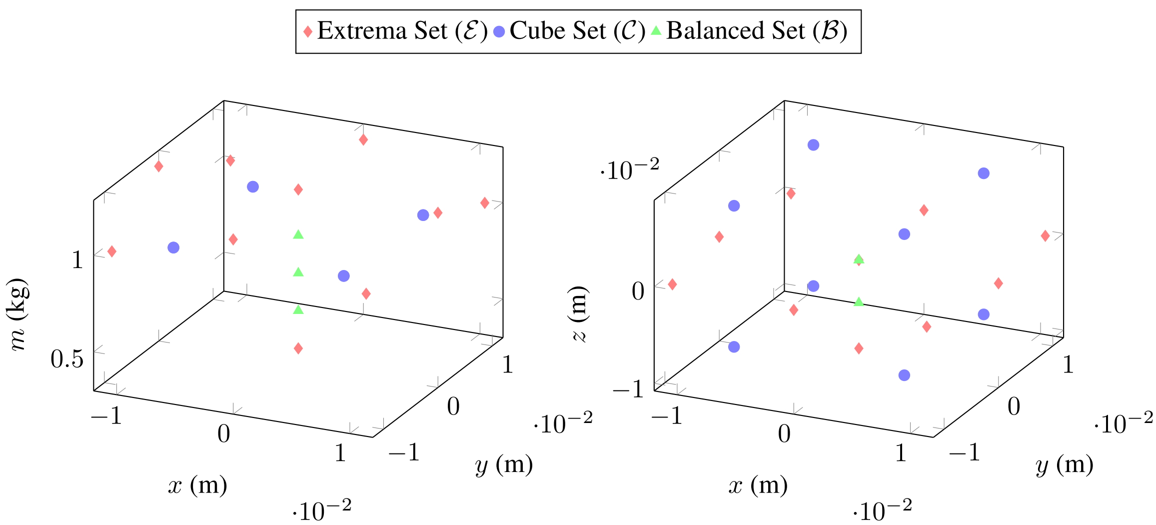

Figure 3.8: Mass and COM coordinates for each test point set.

m	$\boldsymbol{r}$	Material Matrix	3D Preview
		Extrema Set ($\mathcal{E}$)	
1.204	$\begin{bmatrix}0.000 & 0.000 & -0.009\end{bmatrix}$	$\begin{bmatrix}\begin{bmatrix}S & A\\ W & S\end{bmatrix} \begin{bmatrix}W & W\\ A & W\end{bmatrix}\end{bmatrix}$	
1.204	$\begin{bmatrix}0.012 & 0.000 & -0.000\end{bmatrix}$	$\begin{bmatrix}\begin{bmatrix}W & W\\ S & A\end{bmatrix} \begin{bmatrix}W & W\\ A & S\end{bmatrix}\end{bmatrix}$	
1.204	$\begin{bmatrix}0.000 & 0.012 & -0.000\end{bmatrix}$	$\begin{bmatrix}\begin{bmatrix}W & S\\ W & A\end{bmatrix} \begin{bmatrix}W & A\\ W & S\end{bmatrix}\end{bmatrix}$	
1.204	$\begin{bmatrix}-0.012 & 0.000 & -0.000\end{bmatrix}$	$\begin{bmatrix}\begin{bmatrix}A & S\\ W & W\end{bmatrix} \begin{bmatrix}S & A\\ W & W\end{bmatrix}\end{bmatrix}$	
1.204	$\begin{bmatrix}0.000 & -0.012 & -0.000\end{bmatrix}$	$\begin{bmatrix}\begin{bmatrix}A & W\\ S & W\end{bmatrix} \begin{bmatrix}S & W\\ A & W\end{bmatrix}\end{bmatrix}$	
0.380	$\begin{bmatrix}0.000 & 0.000 & 0.000\end{bmatrix}$	$\begin{bmatrix}\begin{bmatrix}W & W\\ W & W\end{bmatrix} \begin{bmatrix}W & W\\ W & W\end{bmatrix}\end{bmatrix}$	
1.009	$\begin{bmatrix}0.011 & 0.011 & -0.000\end{bmatrix}$	$\begin{bmatrix}\begin{bmatrix}W & W\\ W & S\end{bmatrix} \begin{bmatrix}W & W\\ W & S\end{bmatrix}\end{bmatrix}$	
1.009	$\begin{bmatrix}-0.011 & -0.011 & 0.000\end{bmatrix}$	$\begin{bmatrix}\begin{bmatrix}S & W\\ W & W\end{bmatrix} \begin{bmatrix}S & W\\ W & W\end{bmatrix}\end{bmatrix}$	
1.009	$\begin{bmatrix}0.011 & -0.011 & 0.000\end{bmatrix}$	$\begin{bmatrix}\begin{bmatrix}W & W\\ S & W\end{bmatrix} \begin{bmatrix}W & W\\ S & W\end{bmatrix}\end{bmatrix}$	
1.009	$\begin{bmatrix}-0.011 & 0.011 & 0.000\end{bmatrix}$	$\begin{bmatrix}\begin{bmatrix}W & S\\ W & W\end{bmatrix} \begin{bmatrix}W & S\\ W & W\end{bmatrix}\end{bmatrix}$	

Table 3.4: Table of all test point configurations,

m	$\boldsymbol{r}$	Material Matrix	3D Preview
		Cube Set ($\mathcal{C}$)	
0.987	$[-0.007 \quad -0.007 \quad -0.007]$	$\left[\begin{bmatrix} S & A \\ A & W \end{bmatrix}\begin{bmatrix} A & W \\ W & W \end{bmatrix}\right]$	
0.987	$[-0.007 \quad 0.007 \quad -0.007]$	$\left[\begin{bmatrix} A & S \\ W & A \end{bmatrix}\begin{bmatrix} W & A \\ W & W \end{bmatrix}\right]$	
0.987	$[0.007 \quad -0.007 \quad -0.007]$	$\left[\begin{bmatrix} A & W \\ S & A \end{bmatrix}\begin{bmatrix} W & W \\ A & W \end{bmatrix}\right]$	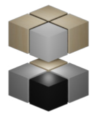
0.987	$[0.007 \quad 0.007 \quad -0.007]$	$\left[\begin{bmatrix} W & A \\ A & S \end{bmatrix}\begin{bmatrix} W & W \\ W & A \end{bmatrix}\right]$	
0.987	$[-0.007 \quad -0.007 \quad 0.007]$	$\left[\begin{bmatrix} A & W \\ W & W \end{bmatrix}\begin{bmatrix} S & A \\ A & W \end{bmatrix}\right]$	
0.987	$[-0.007 \quad 0.007 \quad 0.007]$	$\left[\begin{bmatrix} W & A \\ W & W \end{bmatrix}\begin{bmatrix} A & S \\ W & A \end{bmatrix}\right]$	
0.987	$[0.007 \quad -0.007 \quad 0.007]$	$\left[\begin{bmatrix} W & W \\ A & W \end{bmatrix}\begin{bmatrix} A & W \\ S & A \end{bmatrix}\right]$	
0.987	$[0.007 \quad 0.007 \quad 0.007]$	$\left[\begin{bmatrix} W & W \\ W & A \end{bmatrix}\begin{bmatrix} W & A \\ A & S \end{bmatrix}\right]$	

Table 3.5

m	$\boldsymbol{r}$	Material Matrix	3D Preview
		Balanced Set ($\mathcal{B}$)	
0.575	$[0.000 \quad 0.000 \quad 0.000]$	$\left[\begin{bmatrix} A & W \\ W & W \end{bmatrix}\begin{bmatrix} W & W \\ W & A \end{bmatrix}\right]$	
0.771	$[0.000 \quad 0.000 \quad -0.004]$	$\left[\begin{bmatrix} A & W \\ A & A \end{bmatrix}\begin{bmatrix} W & A \\ W & W \end{bmatrix}\right]$	
0.966	$[0.000 \quad 0.000 \quad 0.000]$	$\left[\begin{bmatrix} A & A \\ W & A \end{bmatrix}\begin{bmatrix} A & W \\ A & A \end{bmatrix}\right]$	

Table 3.6

3.5 Discussion & Conclusion

3.5.1 Future Work

3.5.1.1 Payload with Improved COM Range

As mentioned in 3.4.1, the COM range of the configurable payload is very small. Similarly to the mass range, the COM range could be increased by the use of denser and lighter materials. However, with the current design, it is not possible to increase the COM range by a significant amount. This is due to the small offset distance of the COM of each material cube, only 17.5 mm from the geometric centroid of the payload. A design that could increase the maximum offset distance would therefore increase the COM range significantly. One proposal would be to use a rod with a mass on one end and a handle for the grippers on the other. The mass material, thickness, and length of the rod could then be varied to adjust the mass and COM of the payload. Since the gripper can rotate $360°$ with the chosen robot arm, any COM can be simulated within a annulus shaped configuration space around $z = 0$ for a given mass, but could be extruded to an annular cylinder if some mechanism was used to vary the z element of the COM (asymmetric masses, rod sliders on the handle, etc.). If two rods either side of the handle are used, the annuli become disks and cylinders respectively, allowing for "balanced" payloads, as can be seen in figure 3.9. This is an advantage over the original design, and eliminates the need for any kind of search algorithm for the COM, since it could be found analytically for a given mass using polar coordinates, where the *radius* is the rod length and the *azimuth* is the gripper rotation angle, though it must be noted the mass and maximum rod length will determine the available range of values for the COM.

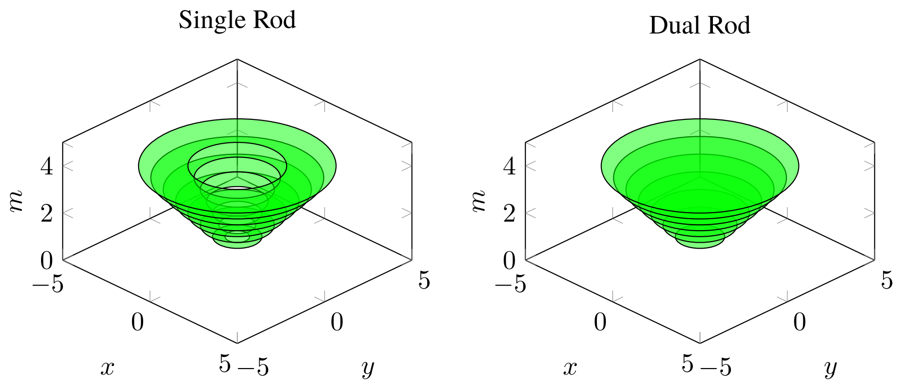

Figure 3.9: Example configuration space for the new configurable payload design, where $z = 0$.

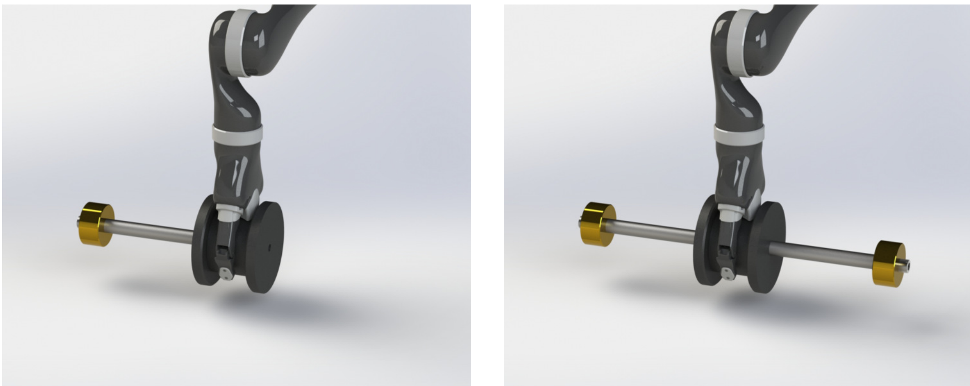

Figure 3.10: Renders of a concept design for the new configurable payload, with a single rod and dual rod configuration.

3.5.1.2 Dynamic COM Implementation: Fluid Filled Container

Not all payloads that a robot may pick up are solid objects, some may have COM that shift during transit due to external disturbances. Generally any container partially filled with either loose material or fluid, such as a bottle or sack, could have a so-called "dynamic" COM. Therefore, a container partially filled with fluid, with a specific viscosity and mass would be a suitable simulacrum for these kinds of payloads. The robot arm could then shake the container from side to side briefly to simulate a disturbance, creating a standing wave inside the container that would have an effect on the COM.

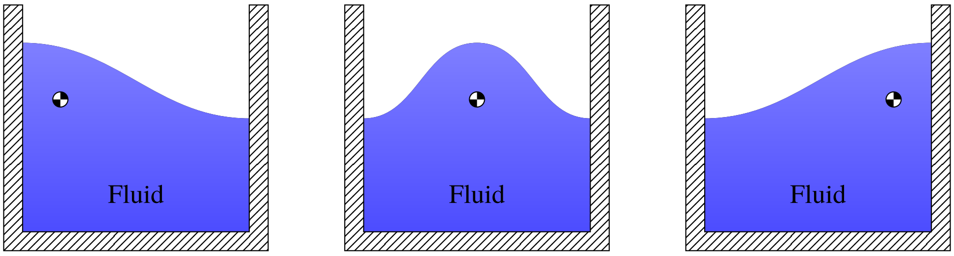

Figure 3.11: Diagram on the COM dynamics of a fluid filled container. If the container is disturbed, a standing wave forms inside the container which causes the COM to oscillate.

3.5.2 Conclusion

This work has outlined the design and implementation of a configurable payload that is suitable for the experiments in chapter **??**. Using this payload, a range of objects with different mass and COM can be emulated in order to generate a wide range of experimental data.

References

[1] *Kinova mico ™robotic arm 4dof specifications*, 1.2, Kinova, Inc., Apr. 2018. [Online]. Available: `https://drive.google.com/file/d/1xCmpqSDMZvKU4IypSaXBLIEX6p7pigGr/view`.

[2] S. Kirkpatrick, C. D. Gelatt, and M. P. Vecchi, “Optimization by simulated annealing,” *science*, vol. 220, no. 4598, pp. 671–680, 1983.

[3] P. Serafini, “Simulated annealing for multi objective optimization problems,” in *Multiple criteria decision making*, Springer, 1994, pp. 283–292.

Chapter 4

Investigating the use of a 2DOF Pendulum Tail for Compensating for Instability when Carrying a Payload

In this chapter, the design of the static rig is outlined, made up of a base, a robotic arm, the configurable payload from chapter **??**, *a 2 DOF "inverted pendulum" tail driven by two brushless motors using a bevel gear arrangement, and four load cells used to calculate the COP. N cost functions for stability are then derived from the COP data when the payload is being lifted by the arm. An experimental trajectory is described which replicates the motions of a mobile robot moving and object from one location to another. A simple proportional controller is then developed and simulated, and its efficacy is compared with experimental results from the constructed rig for each test point set in chapter* **??**. *The discussion then examines the efficacy of the chosen design and actuation method for the robotic tail, and its limitations and potential improvements, as well as examining the ability of the configurable payload to generate a suitably wide range of test points, given the variation in the motion of the tail for each point.*

4.1 Introduction

As mentioned in chapter **??**, the primary question of this research is to quantify the efficacy of a robotic tail for maintaining the stability of a mobile robot when carrying a payload. While the ultimate verification for this question would be to attach a tail to a mobile robot and engage in field trials, carrying objects in a close simulacrum to a real operating environment, a simpler and more flexible approach is to use a static rig which can measure a "virtual" static stability using the COP. By comparing the measurement to a robot's known stability region (typically referred to as the *support polygon*[1]) and initial center of mass, it is possible to determine if a specific mobile robot would remain statically stable without having to topple a mobile robot, and risk equipment damage.

However, demonstrating an improvement in a discrete set of pass/fail stability tests based on specific mobile robots is not necessary to answer the research question. Instead, a continuous approach can be used, which considers stability as a cost function rather than a binary result. This has the advantage of being able to quantify *how* stable the experiment is, and the magnitude of dynamic forces a given robot could withstand. The smaller the cost and the larger the support polygon, the greater the magnitude, depending on the distance to the polygon boundary in a specific direction.

4.2 Experiment Design

The static rig can be abstractly defined as follows: a rectangular base of dimensions $\begin{bmatrix} b_x & b_y \end{bmatrix}$ centred around the origin where the force is measured at each vertex to create a matrix $\boldsymbol{F} \in \mathbb{R}^{2\times 2}$ where each element is the force measured at the corner of the rectangle defined by its position in the matrix. The robot arm and tail are positioned along the origin X axis at a_y and $-t_y$ on the Y axis, and a_z and t_z on the Z axis. The tail is a rod attached to a 2 DOF joint, with the orientation controlled by input angles $\boldsymbol{\theta}$. The robot arm is a 4 DOF design with a pair of grippers to pick up a payload, with the input angles $\boldsymbol{q}$.

$\boldsymbol{F}$ can then be used to measure the Center of Pressure, defined as the the point of application of the GRF vector. [2] gives the following equation to calculate the COP:

$$
\begin{aligned}
\boldsymbol{F} &= \begin{bmatrix} f_{x,y} & f_{-x,y} \\ f_{x,-y} & f_{-x,-y} \end{bmatrix} \\
CP\left(\boldsymbol{F}\right) &= \begin{bmatrix} \dfrac{b_x\left(\left(f_{11}+f_{21}\right)-\left(f_{12}+f_{22}\right)\right)}{\sum_{i=1}^{2}\sum_{j=1}^{2} f_{ij}} \\ \dfrac{b_y\left(\left(f_{11}+f_{12}\right)-\left(f_{21}+f_{22}\right)\right)}{\sum_{i=1}^{2}\sum_{j=1}^{2} f_{ij}} \end{bmatrix}
\end{aligned}
\tag{4.1}
$$

Where $f_{\square,\square}$ refers to the location of the load measurement on figure 4.1.

Four load cells were used instead of a force plate, which would have likely resulted in a more accurate measurement, in order to replicate what would be practical to measure on a mobile robot. Attaching load cells to each leg or wheel mount on a mobile robot would be fairly trivial and cost effective, dividing the body in order to insert a force plate or dynamometer would be difficult ad costly. [2], [3] compare a similar mechanism using the Wii Fit™ Balance Board, and was able to achieve a COP repeatability to within 1.5 mm.

$$CP\left(\boldsymbol{F}\right) = \frac{m_b \boldsymbol{r}_b + m_a \boldsymbol{r}_a(\boldsymbol{q}) + m_p \boldsymbol{r}_p(\boldsymbol{q}) + m_t \begin{bmatrix} l_t \cos\theta_1 \\ -t_y + l_t \cos\theta_2 \end{bmatrix}}{m_b + m_a + m_t} \tag{4.2}$$

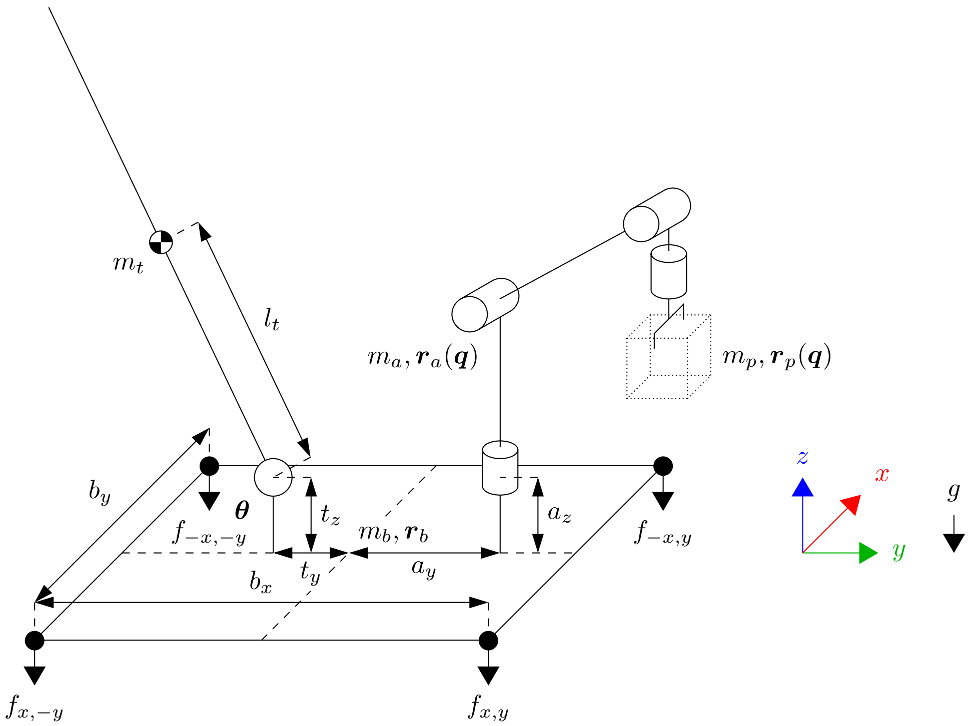

Figure 4.1: Free body diagram of the static test setup.

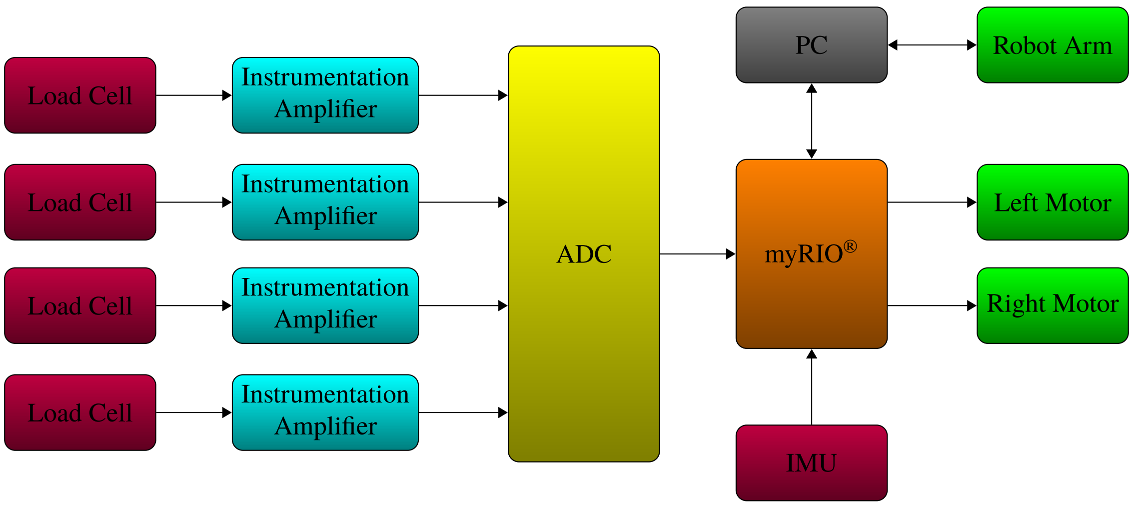

Figure 4.2: System diagram of the static rig.

4.2.1 Base

The base consists of two pairs of steel plates orthogonal to each other, separated by load cells and rubber vibration dampers. The lower plates are clamped to a sturdy table at the four positions indicated in figure 4.3, and a pair of shallow Unistrut® channels are bolted between the upper plates. The plates for the robot arm and tail are then secured to the rig with nuts that slot into the channels, allowing them to be shifted along the Y axis so a_y and t_y can be adjusted.

The load cells are Omega™ LCM204 with a range of ± 200N, connected to Fylde FE-359-TA instrumentation amplifiers that fed the amplified signal to an Analog Devices AD7606 Analog to Digital Converter (ADC), which was connected to the National Instruments (NI) myRIO®. A separate ADC was chosen due the limited number of differential analog inputs on the myRIO®, with only two on the MSP connector [4]. The chosen ADC also had a greater resolution of 16 bits [5] than the built-in myRIO® ADC of 12 bits [4].

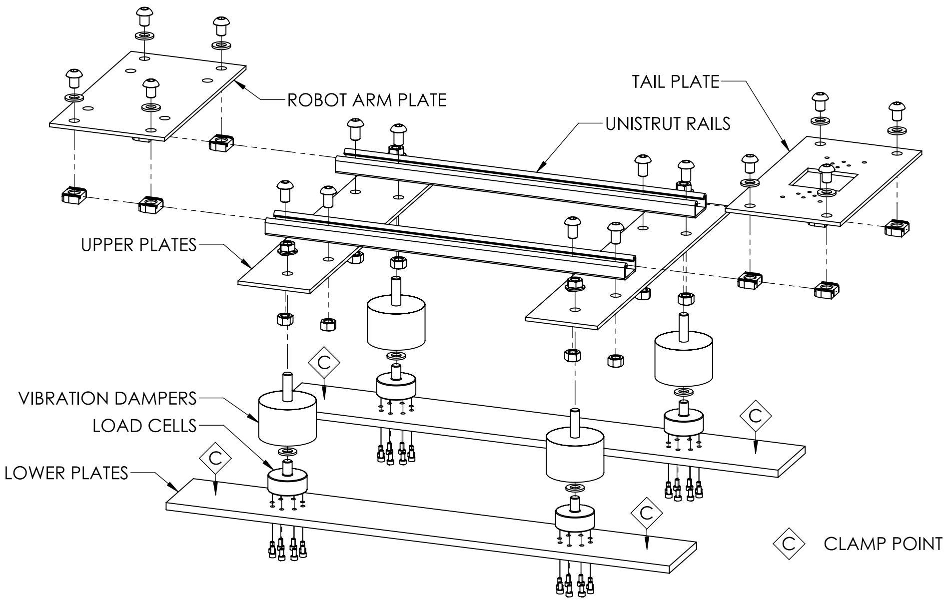

Figure 4.3: Exploded schematic of the base of the static rig, with important components labelled and clamping points marked.

4.2.2 Robot Arm

The robot arm is a Kinova™ MICO^2 4DOF model with a KG-2 gripper end effector. It can carry a maximum payload of 2 kg when fully extended, though in experimental conditions for the configurable payload designed in chapter 3 the friction force between the grippers and textured surface of the container was insufficient for loads much lower than this limit. It is attached to the base using a mount which is bolted to the robot arm plate.

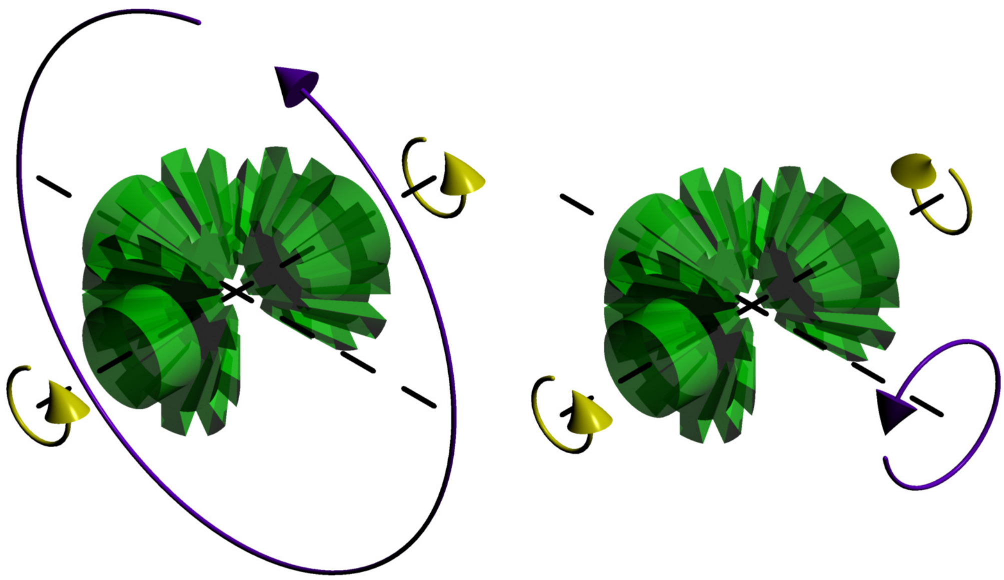

Figure 4.4: Visualisation of the bevel gear system. When both driving gears turn in the same direction, the driven gear rotates around the driving gears axis. When the driving gears turn in opposite directions, it rotates around its own axis.

4.2.3 Robot Tail

While the actuator designed in chapter **??** proved that it could be a successful actuation system for the robot tail, it was not considered mature enough to be applied to this experiment. Instead, a simpler design was used, based on the common "inverted pendulum" designs used in many of the publications found in chapter 2, with a 2 DOF joint attached to a rod with a mass on the end. In particular, the design from [6] which used a 3 way bevelled gear system to create a 2 DOF joint, which allowed both motors to be mounted to the base, increasing the available tail torque. This design works as shown in figure 4.4, where rotating both motors in the same direction rotates the tail joint around the axis of the *driving* gears connected to the motor shafts, and rotating the motors in opposite directions rotates the tail in the axis of the *driven* gear attached to the tail.

In order to translate motor rotations to tail motion, the following equation can be used, where $\phi = \begin{bmatrix}\phi_1 & \phi_2\end{bmatrix}^\intercal$ are the motor angles:

$$\dot{\boldsymbol{\phi}} = \begin{bmatrix} 1 & -1 \\ -1 & -1 \end{bmatrix} \dot{\boldsymbol{\theta}} \tag{4.3}$$

4.2.4 Test Sequence

The experiment test sequence is designed to replicate the actions of a mobile robot that is moving an object from one place to another. The robot arm grasps the payload and lifts it off the ground plane, then holds it for a predetermined period of time, before placing it back down on the ground plane and releasing it.

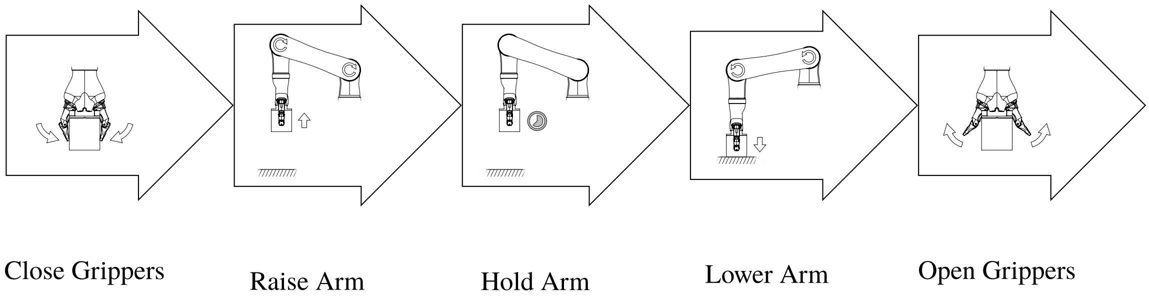

Figure 4.5: Trajectory sequence of the robot arm and payload.

This sequence is repeated twice for each test point in the sets designed in chapter 3, once with no tail attached to the rig as a control, and once with the active tail attached to the rig. The area of interest for the research is the "carry' section of the experiment, between the *Raise Arm* and *Lower Arm* stages, specifically when the payload is not in contact with the ground plane.

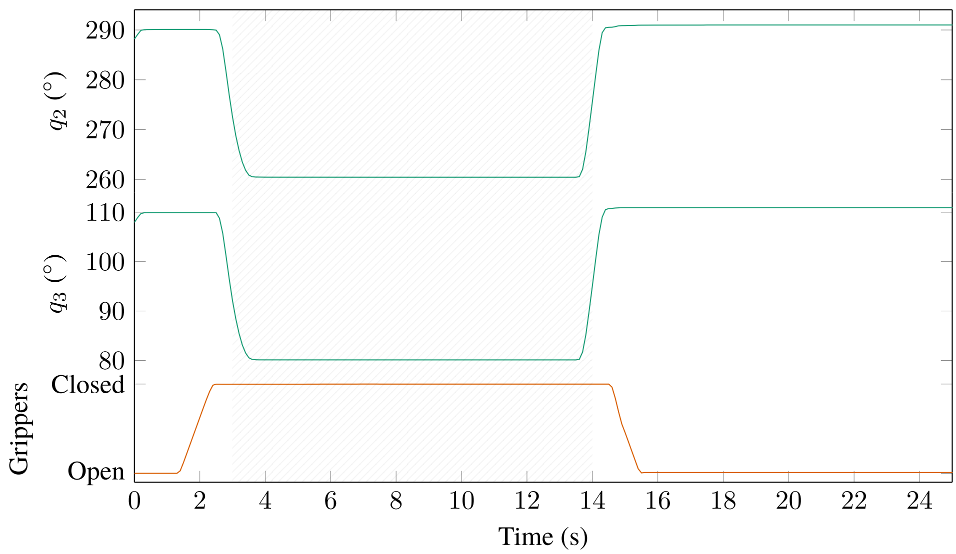

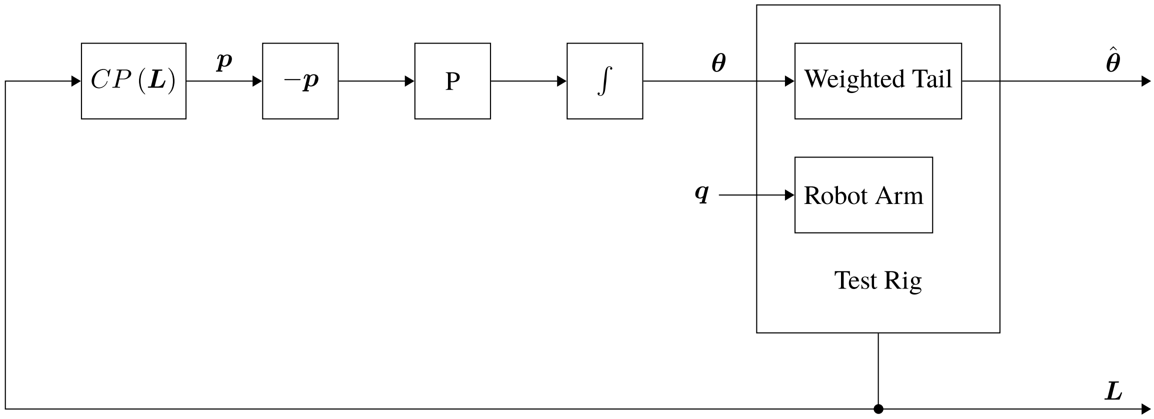

Figure 4.6: Simulation block diagram.

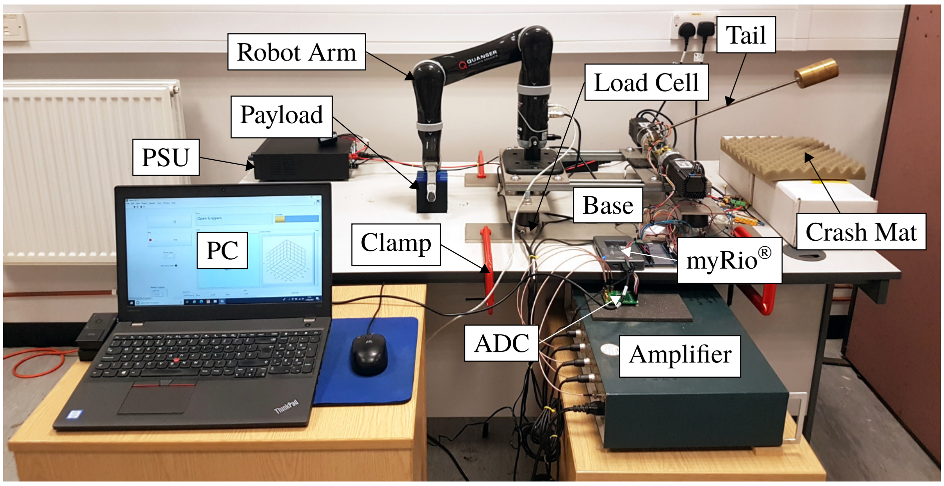

Figure 4.7: Labelled photograph of the static rig.

4.3 Simulation

4.3.0.1 Control System

4.4 Experiments

4.4.1 Design

4.4.1.1 Control System

$$\begin{aligned} \boldsymbol{F} &= \begin{bmatrix} f_{x,y} & f_{-x,y} \\ f_{x,-y} & f_{-x,-y} \end{bmatrix} \\ CP(\boldsymbol{F}) &= \begin{bmatrix} \dfrac{l_x\left((f_{11}+f_{21})-(f_{12}+f_{22})\right)}{\sum_{i=1}^{2}\sum_{j=1}^{2} f_{ij}} \\ \dfrac{l_y\left((f_{11}+f_{12})-(f_{21}+f_{22})\right)}{\sum_{i=1}^{2}\sum_{j=1}^{2} f_{ij}} \end{bmatrix} \end{aligned} \tag{4.4}$$

Equation from [6]:

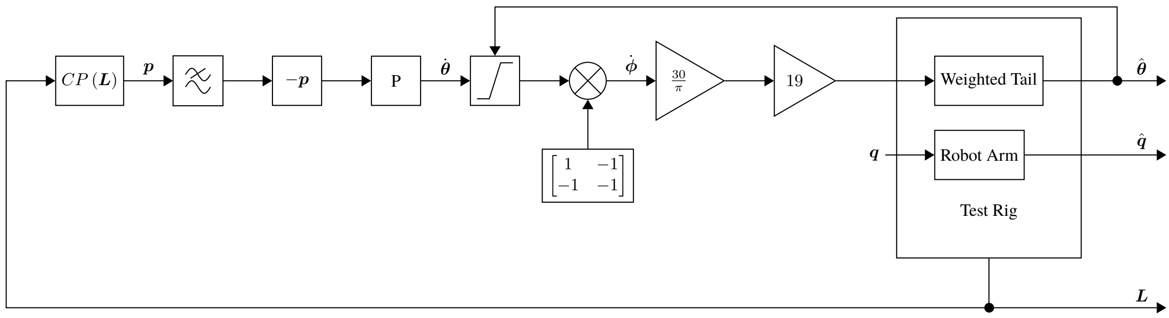

Figure 4.8: Block diagram of the control system.

4.4.2 Results and Performance

For each test point, 20 experiments were run, 10 *control* experiments without the tail attached, and 10 *tail* experiments with the feedback controlled tail. The mean values for the 10 experiments were then taken as the performance measurements, with the minimum and maximum values considered as the measurement error.

In order to provide a fair comparison between the control and tail experiments, a perfectly balanced initial condition is assumed for the control experiments. This was done by offsetting the COP data by the value of the initial condition.

The following data was taken from each run of the experiment, where each symbol represents a scalar or vector time series $\{x_t; t \in \mathbb{R}^+ \mid t \leq n\}$ where n is the final sample time:

4.4.2.1 Center of Pressure

One option is to measure the minimum

This point may not exist within the time series

4.4.2.2 Vibration Analysis

4.4.2.3 Payload and Tail Angle Regression Analysis

To examine the effects of a varying the payload mass and COM on the tail, a regression study was conducted comparing mass and COM *inputs* to tail angle *outputs*, specifically the peak angle output measured by the maximum magnitude function, where $\boldsymbol{\theta}$ represents the vector of tail angle measurements from the experiment:

$$\wedge(\boldsymbol{\theta}) = \begin{cases} \max \boldsymbol{\theta} & |\max \boldsymbol{\theta}| \leq |\min \boldsymbol{\theta}| \\ \min \boldsymbol{\theta} & |\max \boldsymbol{\theta}| > |\min \boldsymbol{\theta}| \end{cases} \tag{4.5}$$

Figure **??** shows the correlations between the maximum magnitude of the tail on both pitch and roll axes, and the mass and corresponding COM of the payload. A change in the x axis

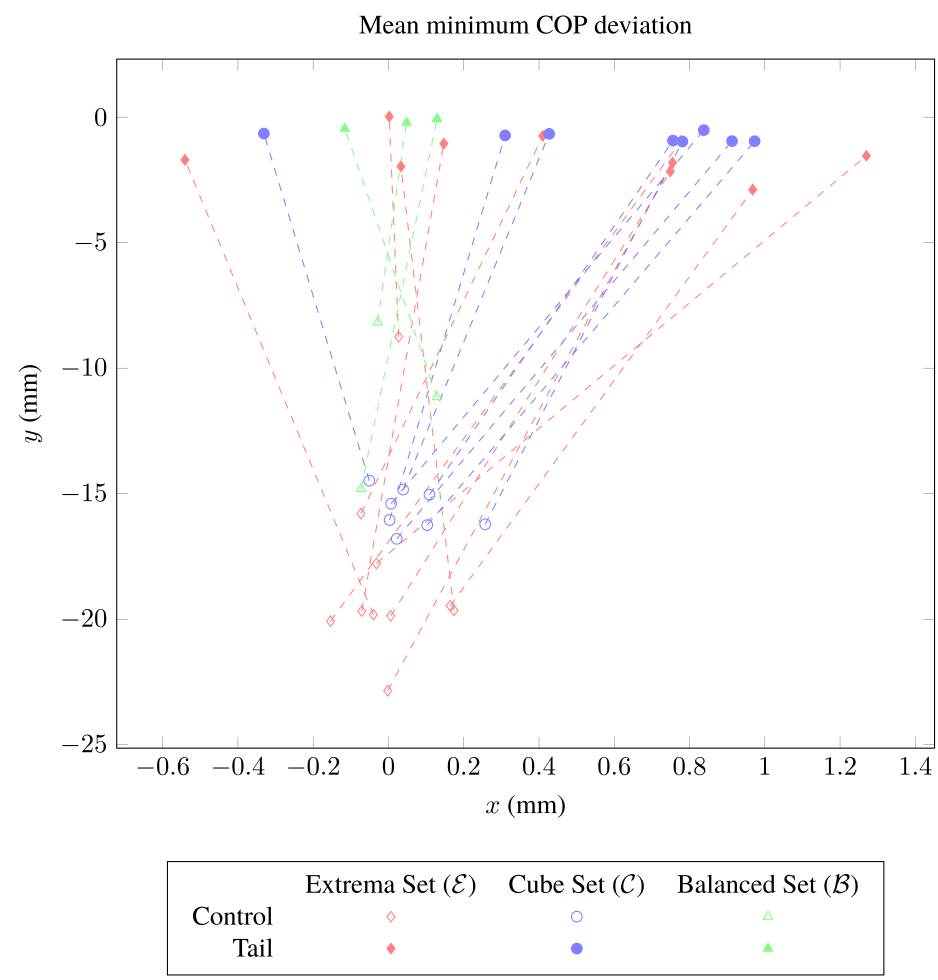

Figure 4.9: Graph of the mean COP during the *carry* phase of the experiment.

of the COM would only affect the roll, and the y axis would only affect the pitch, but a change in mass would effect both, though the y axis to a much greater degree.

The results show that there is a strong correlation ($p = 6.056 \times 10^{-13}$) between the payload mass and the pitch maximum magnitude of the tail of $1.046\,\mathrm{rad\,kg^{-1}}$. There are also weaker correlations ($p = 0.127$ and $p = 0.081$) between the COM x and y axis and the pitch maximum magnitude of the tail at $0\,\mathrm{rad\,mm^{-1}}$ and $0\,\mathrm{rad\,mm^{-1}}$ respectively. While these are too large to be considered a statistical certainty ($p > 0.05$), they do still suggest a approximately 90% probability there was an effect, assuming the mean values from each test point are accurate.

4.5 Discussion and Conclusion

A major issue with the experiments that likely prevented the collection of more accurate data and more stable control of the tail was the vibration of the tail shaft. This could potentially be alleviated by using a stiffer material for the shaft, or using a shaft of a larger diameter. However, this would likely increase the mass of the tail shaft, or would require more specialised materials to be sought.

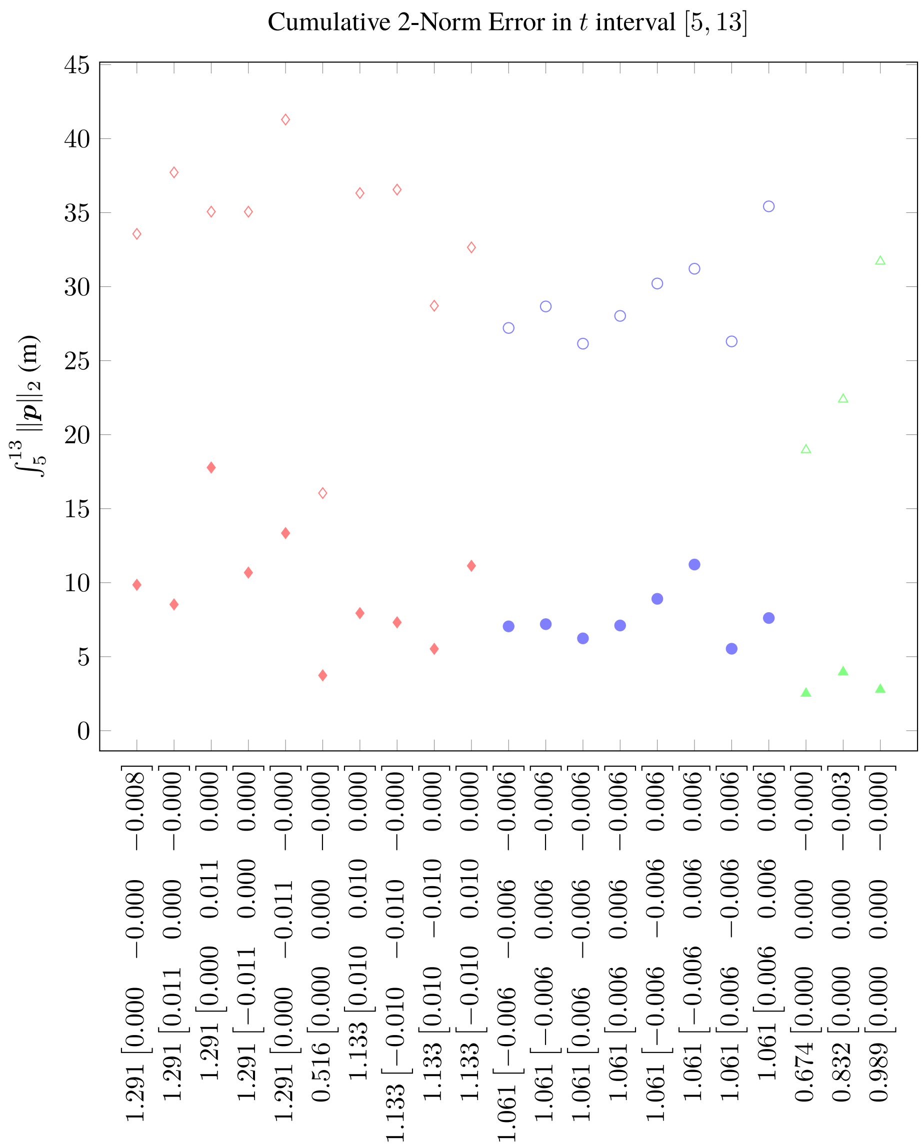

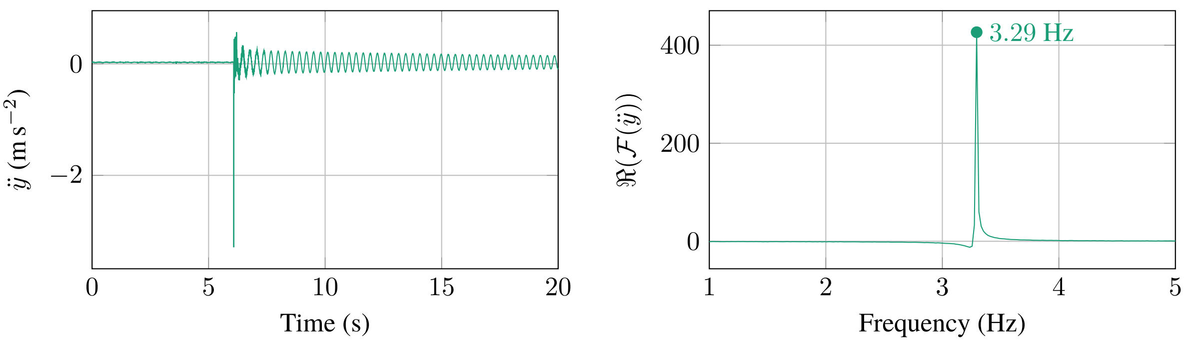

Figure 4.10: Resonant frequency of the tail calculated from accelerometer data captured during an impact with a steel hammer. The left graph is the accelerometer data, and the right graph is the real part from a real DFT on the data.

References

[1] R. B. McGhee and A. A. Frank, "On the stability properties of quadruped creeping gaits," *Mathematical Biosciences*, vol. 3, pp. 331–351, 1968.

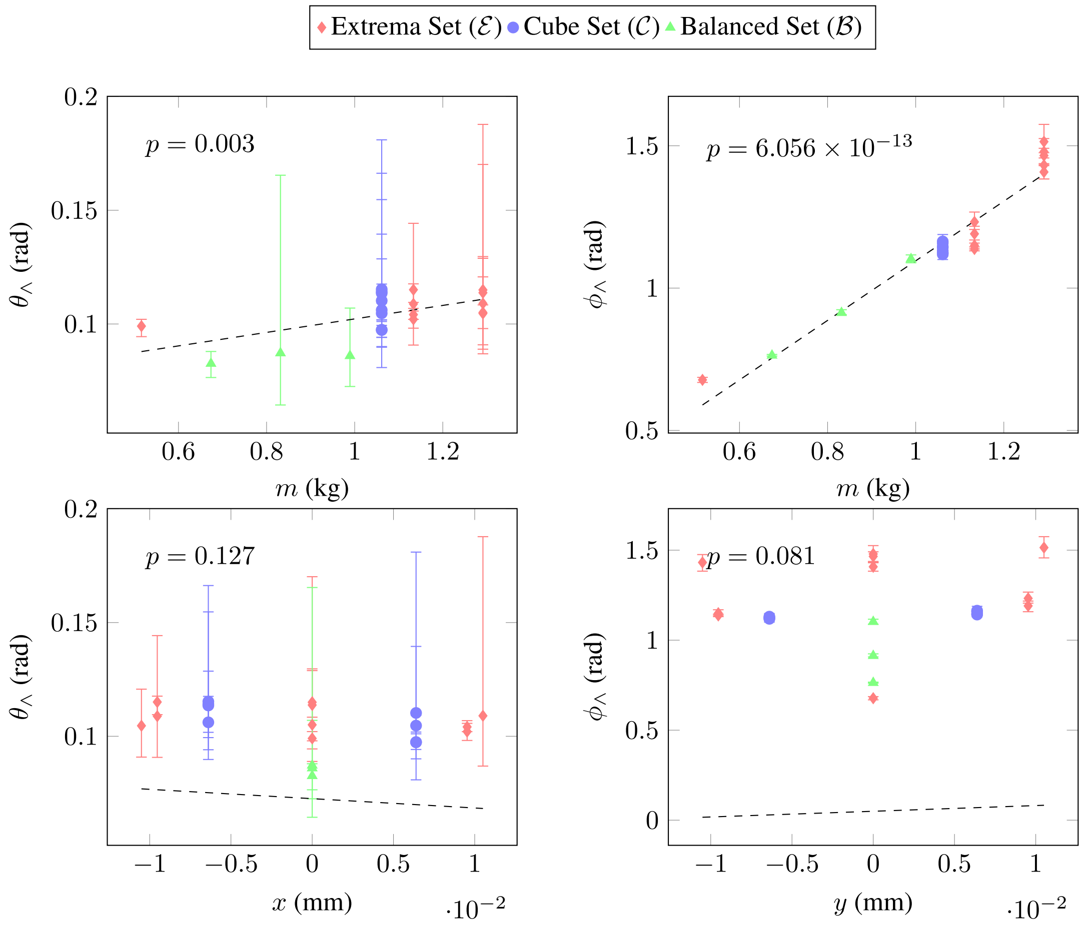

Figure 4.11

[2] H. L. Bartlett, L. H. Ting, and J. T. Bingham, "Accuracy of force and center of pressure measures of the wii balance board," *Gait & posture*, vol. 39, no. 1, pp. 224–228, 2014.

[3] J. M. Leach, M. Mancini, R. J. Peterka, T. L. Hayes, and F. B. Horak, "Validating and calibrating the nintendo wii balance board to derive reliable center of pressure measures," *Sensors*, vol. 14, no. 10, pp. 18 244–18 267, 2014.

[4] *NI myRIO-1900 user guide and specifications*, National Instruments, May 2016.

[5] *AD7606/AD7606-6/AD7606-4 data sheet*, version F, Analog Devices, Apr. 2020.

[6] A. Patel and E. Boje, "On the conical motion of a two-degree-of-freedom tail inspired by the cheetah," *IEEE Transactions on Robotics*, vol. 31, no. 6, pp. 1555–1560, 2015. DOI: 10.1109/TRO.2015.2495004.

Appendices